

# GRASSMANNIAN OPTIMIZATION FOR ONLINE TENSOR COMPLETION AND TRACKING IN THE T-SVD ALGEBRA

KYLE GILMAN\* AND LAURA BALZANO†

**Abstract.** We propose a new streaming algorithm, called TOUCAN, for the tensor completion problem of imputing missing entries of a low-tubal-rank tensor using the recently proposed tensor-tensor product (t-product) and tensor singular value decomposition (t-SVD) algebraic framework. We also demonstrate TOUCAN’s ability to track changing free submodules from highly incomplete streaming 2-D data. TOUCAN uses principles from incremental gradient descent on the Grassmann manifold of subspaces to solve the tensor completion problem with linear complexity and constant memory in the number of time samples. We compare our results to state-of-the-art tensor completion algorithms in real applications to recover temporal chemo-sensing data and MRI data under limited sampling.

**Key words.** t-SVD, t-product, Grassmannian optimization, online tensor completion, MRI reconstruction

**AMS subject classifications.** 15A69, 15A83, 49Q99, 68W27, 90C26

**1. Introduction.** Modern data are increasingly high-dimensional and multiway, increasing the storage and computational burden of signal processing algorithms. Many practical applications collect data over multiple modalities, such as chemo-sensing experiments that record sensor readings from dozens of channels in hundreds of experiments over thousands of time series, or hyperspectral imaging (HSI), which captures dozens or even hundreds of images in narrow, adjacent spectral bands for each frame [38]. Time-sequential HSI, i.e., hyperspectral video (HSV), with hundreds of spectral bands and megapixel spatial resolution requires images to be recorded at the order of 10 G pixels per second. It is currently infeasible to process this type of high-rate data in real time applications [15]. Batch processing of large-scale tensor data quickly becomes computationally intractable, and even storing these tensors is problematic as the memory requirements grow rapidly with the number and size of the tensor modes. Additional challenges include large numbers of missing tensor entries and streaming multiway data that needs to be processed on the fly.

To address these concerns, there is extensive recent literature studying low-dimensional tensor decompositions and fast algorithms for computing them. These decompositions provide a low-memory model approximation to tensor data that can be used for compression and interpolating missing entries. Several algebraic frameworks exist for the analysis and decomposition of tensors, each with their own notion of tensor rank. In this paper, we consider sampling and recovery of 3-way tensors using the algebraic framework of the t-SVD [11, 21, 30]. Three-way tensors are treated as linear operators over the space of oriented matrices and group rings of fibers under the t-product multiplicative operator. Using this framework, one obtains an SVD-like factorization referred to as the tensor-SVD (t-SVD) with a defined notion of rank referred to as the tubal-rank. A key property of the t-SVD is the optimality of the truncated t-SVD for data approximation under the Frobenius norm measure [41].

The t-SVD has been well-studied in exact tensor recovery [41], image and video inpainting [42, 44, 26], hyperspectral data [13, 14], and solving tensor robust PCA problems for video foreground/background separation [9, 43]. However, most existing

---

\*University of Michigan, Ann Arbor, MI (kgilman@umich.edu).

†University of Michigan, Ann Arbor, MI (girasole@umich.edu).

t-SVD based methods are batch methods that require all of the data to be stored in memory at computation time and/or require the computation of multiple SVDs. This is very time-consuming and inefficient for large-scale data.

We therefore propose a new algorithm called TOUCAN (**T**ensor **R**ank-**O**ne **U**ppdate on the **C**omplex Grassmannian) to recover low-rank tensor data from streaming, highly-incomplete multiway data with incremental gradient descent on the product manifold of low-rank matrices in the Fourier domain using the framework of the t-SVD. Our method is online by nature, avoids the SVD, maintains orthonormality on the tensor Grassmann manifold, and scales linearly in computation with the number of samples. We compare our method to batch t-SVD methods and streaming methods in the CANDECOMP/PARAFAC (CP) algebra. We show our method’s ability to track dynamically time-varying low-rank free submodules from streaming two-way data in time-lapse video and undersampled functional magnetic resonance imaging (fMRI) data. Additionally, our method can be extended to higher-order tensors by slightly modifying our derivations to the order- $p$  t-SVD [31].

### 1.1. Organization of this paper.

- Section 3: Since our tensor factorization algorithm is based on the t-product [11], we cover the background for this decomposition in detail in this section. At a high level, the t-product is convolutional and so can be performed by a product in the Fourier domain.
- Section 4 proposes our tensor completion method, summarized in Algorithm 4.1.
- Section 5: Experimental results are given for synthetic data, time-lapse video, and MRI array data in this section.

**2. Related Work.** It is well known that low-rank decompositions of highly undersampled matrix data, with certain assumptions of incoherent left and right singular vectors from the Singular Value Decomposition (SVD) and random sampling patterns, can be exploited to recover missing data by solving a convex optimization program [7]. This setting treats matrix data (a 2-way tensor) as a linear operator over a vector space and defines the rank of the matrix via its minimal decomposition into a sum of rank-1 matrices [41]. However, multiway data often contains correlations or interactions between modes of the tensor that would otherwise be destroyed if the tensor is flattened into a matrix [24]. More sophisticated algebraic techniques are required to analyze these special structures.

The work in [41] solves the exact tensor completion problem under the t-SVD algebra in a batch way using the tensor nuclear norm, a convex relaxation of tensor tubal-rank. The algorithm involves solving a convex program on each frontal slice of the tensor in the Fourier domain, which provably recovers the missing tensor entries given certain incoherence conditions. The authors of [44] propose a different algorithm using a tensor factorization model under the t-product for rapid, efficient optimization. Both of these algorithms can only complete batch tensor data and cannot handle streaming multiway data. Little work has been done to extend online matrix completion methods to the case of multiway tensor data using the t-SVD framework, apart from the work in [43] which proposed an online tensor robust principal component analysis algorithm. However, this method cannot predict missing tensor values and does not estimate an orthonormal factorization. The work in [34] proposed an online tensor completion algorithm using the tensor nuclear norm for low-tubal-rank tensors, but it must compute a t-SVD for each update.

One of the most widely used tensor decompositions is the CANDE-

COMP/PARAFAC (CP) factorization which finds a sum of rank-1 outer products that best compose the tensor where the minimal number of such factors required is referred to as the CP rank [22]. CP is powerful for imputing missing tensor data and also recovering latent factors that describe the tensor along each mode. CP methods often use alternating least squares to update the factor matrices in a nonconvex optimization problem. Several varieties of CP algorithms exist for batch tensor completion such as CP Weighted OPTimization (CP-WOPT) [2, 19] and Tensor Alternating Least Squares (TenALS) [19], both which have good scalability to large tensors. Kolda and Hong [23] also proposed using stochastic gradients for efficient generalized CP decomposition of large-scale tensors. However there are known computational and ill-posedness issues with the CP model, the foremost issue being that determining the CP rank of a tensor is an NP-hard problem [10]. Unlike the matrix setting, there does not exist a best low-rank CP approximation of a tensor in the Frobenius norm sense [41]. Furthermore, the alternating least squares algorithm is prone to getting stuck in local minima, and so it may be sensitive to initialization or may require a special initialization step.

Newer work in tensor completion has seen the development of several streaming CP tensor completion methods. A prominent streaming version of CP tensor completion was proposed by Mardani et al. [29] using stochastic gradient descent. Kasai [20] proposed another streaming CP tensor completion algorithm with a second-order stochastic gradient descent procedure based on the CP decomposition exploiting recursive least squares for faster convergence than the SGD method in Mardani et al., but at a higher computational cost. The main disadvantage to these streaming CP methods is that they require several hyperparameters that may be difficult to tune or know beforehand. These include a forgetting factor that varies the algorithm’s tracking ability from online mode to purely batch mode, and the regularization parameters that penalize the Frobenius norm of the factor matrices [35]. Setting the appropriate CP rank of the model may also be challenging. Other streaming CP algorithms include [28, 18, 27, 36, 32].

The algorithm proposed in this paper differs from all of these methods in that it can operate in both batch and online modes without a forgetting factor. TOUCAN seeks the best low-rank approximation of a tensor in the Frobenius norm sense under the t-SVD, and is empirically robust to initialization. TOUCAN requires only one hyperparameter—the model rank, which can be more easily determined empirically by inspecting the tubal singular value decomposition of the t-SVD of small batches of data or over the entire batch if feasible. Otherwise, no regularization parameters are needed. This paper builds off the work in [16], giving a full derivation of the algorithm, adding a new algorithm that completes missing tubes of observations, adding theory about conjugate gradient iterations needed in each iteration of our algorithm, and including new and more extensive experiments.

**3. Preliminaries.** The following notation and preliminaries are adopted from the work in [11, 9].

**3.1. Notation.** We denote a three-way tensor as  $\mathcal{A}^{n_1 \times n_2 \times n_3}$  and denote its  $(i, j, k)$ -th entry as  $\mathcal{A}_{ijk}$ . We use  $\mathcal{A}(i, :, :)$ ,  $\mathcal{A}(:, i, :)$ ,  $\mathcal{A}(:, :, i)$  to denote the tensor’s  $i$ -th horizontal, lateral, and frontal slices respectively. Frontal slices are also denoted as  $\mathcal{A}^{(i)}$ .  $\mathcal{A}^*$  denotes the conjugate transpose tensor (defined in Section 2.3). The complex conjugate of a tensor  $\text{conj}(\mathcal{A})$  takes the complex conjugate of each entry of  $\mathcal{A}$ . We denote the Frobenius norm as  $\|\mathcal{A}\|_F = \sqrt{\sum_{ijk} |\mathcal{A}_{ijk}|^2}$ . Any lateral slice of

size  $n_1 \times 1 \times n_3$  is denoted  $\vec{\mathcal{A}}$ , and any  $1 \times 1 \times n_3$  tube along the third-dimension is denoted as  $\vec{t}$ .

**3.2. Discrete Fourier Transform.** Denote the Discrete Fourier Transform (DFT) matrix for operation on a length- $n$  signal as  $F_n \in \mathbb{C}^{n \times n}$  and the DFT of some vector  $v \in \mathbb{R}^n$  as  $\bar{v} = F_n v \in \mathbb{C}^n$ . Note that  $F_n/\sqrt{n}$  is unitary, i.e.  $F_n^* F_n = F_n F_n^* = nI_n$  and  $F_n^{-1} = F_n^*/n$ . The DFT is commonly computed in  $O(n \log n)$  time by the fast Fourier transform (FFT) as  $\bar{v} = \text{fft}(v)$ .

We denote  $\bar{\mathcal{A}} \in \mathbb{C}^{n_1 \times n_2 \times n_3}$  as the result of computing the DFT along the 3<sup>rd</sup> dimension, i.e. performing the DFT on the tubes of  $\mathcal{A}$ . Using the FFT (with indexing in MATLAB notation) we have  $\bar{\mathcal{A}} = \text{fft}(\mathcal{A}, [], 3)$  and similarly by the inverse DFT, we have  $\mathcal{A} = \text{ifft}(\bar{\mathcal{A}}, [], 3)$ .

The block-diagonal matrix  $\bar{A} \in \mathbb{C}^{n_1 n_3 \times n_2 n_3}$  is the matrix with  $n_3$  blocks of size  $n_1 \times n_2$  that are the frontal faces of  $\bar{\mathcal{A}}$ , denoted  $\bar{A}^{(i)} \quad \forall i = 1, \dots, n_3$ , along its diagonal:

$$\bar{A} = \text{bdiag}(\bar{\mathcal{A}}) = \begin{bmatrix} \bar{A}^{(1)} & & & \\ & \ddots & & \\ & & \bar{A}^{(n_3)} & \\ & & & \end{bmatrix}$$

We define the block-circulant matrix of the frontal slices of  $\mathcal{A}$  as  $\text{bcirc}(\mathcal{A})$  where

$$\text{bcirc}(\mathcal{A}) = \begin{bmatrix} A^{(1)} & A^{(n_3)} & \dots & A^{(2)} \\ A^{(2)} & A^{(1)} & \dots & A^{(3)} \\ \vdots & \vdots & \ddots & \vdots \\ A^{(n_3)} & A^{(n_3-1)} & \dots & A^{(1)} \end{bmatrix} \in \mathbb{R}^{n_1 n_3 \times n_2 n_3}$$

From properties of block-circulant matrices,  $\text{bcirc}(\mathcal{A})$  can be block-diagonalized by the DFT

$$(3.1) \quad \bar{A} = (F_{n_3} \otimes I_{n_1}) \cdot \text{bcirc}(\mathcal{A}) \cdot (F_{n_3}^{-1} \otimes I_{n_2})$$

where  $\otimes$  denotes the Kronecker product, and  $(F_{n_3}^{-1} \otimes I_{n_2})/\sqrt{n_3}$  is unitary [9].

Using properties of the Fourier Transform, we give Lemma 3.1, which describes conjugate symmetry of a real-valued signal transformed into the Fourier domain:

LEMMA 3.1. [9] Given  $\mathcal{A} \in \mathbb{R}^{n_1 \times n_2 \times n_3}$ ,

$$\bar{A}^{(1)} \in \mathbb{R}^{n_1 \times n_2} \text{ and } \text{conj}(\bar{A}^{(i)}) = \bar{A}^{(n_3-i+2)}, \quad i = 2, \dots, \lceil \frac{n+1}{2} \rceil.$$

Lemma 3.1 states the conjugate symmetry property for a real-valued signal in the frequency domain using properties from the Fourier transform; this will be useful later for avoiding redundant computations.

**3.3. T-Product and T-SVD.** For  $\mathcal{A} \in \mathbb{R}^{n_1 \times n_2 \times n_3}$  we define the fold and unfold operators [11]:

$$\text{unfold}(A) = \begin{bmatrix} A^{(1)} \\ A^{(2)} \\ \vdots \\ A^{(n_3)} \end{bmatrix} \quad \text{fold}(\text{unfold}(\mathcal{A})) = \mathcal{A}$$

where the `unfold` operator maps  $\mathcal{A}$  to a matrix of size  $n_1 n_3 \times n_2$  and `fold` is its inverse operator.

DEFINITION 3.2 (T-product). [11]: Let  $\mathbf{A} \in \mathbb{R}^{n_1 \times n_2 \times n_3}$  and  $\mathbf{B} \in \mathbb{R}^{n_2 \times l \times n_3}$ . Then the t-product  $\mathbf{A} * \mathbf{B}$  is defined to be a tensor of size  $n_1 \times l \times n_3$ ,

$$(3.2) \quad \mathbf{A} * \mathbf{B} = \text{fold}(\text{bcirc}(\mathbf{A}) \cdot \text{unfold}(\mathbf{B})).$$

The t-product can be understood from several perspectives. First, in canonical domain, a three-way tensor of size  $n_1 \times n_2 \times n_3$  can be thought of as an  $n_1 \times n_2$  matrix whose entries are a tubes lying in the third dimension. The t-product is then analogous to matrix-matrix multiplication but where circular convolution replaces scalar multiplication between the matrix elements. Second, the t-product is equivalent to matrix-matrix multiplication in the Fourier domain, or  $\mathbf{C} = \mathbf{A} * \mathbf{B}$  is equivalent to  $\bar{\mathbf{C}} = \bar{\mathbf{A}}\bar{\mathbf{B}}$  from eq. 3.1. This is shown as follows:

(3.3)

$$\text{unfold}(\mathbf{C}) = \text{bcirc}(\mathbf{A}) \cdot \text{unfold}(\mathbf{B})$$

(3.4)

$$\begin{aligned} &= (F_{n_3}^{-1} \otimes I_{n_1}) \cdot ((F_{n_3} \otimes I_{n_1}) \cdot \text{bcirc}(\mathbf{A}) \cdot (F_{n_3}^{-1} \otimes I_{n_2})) \cdot ((F_{n_3} \otimes I_{n_2}) \cdot \text{unfold}(\mathbf{B})) \\ &= (F_{n_3}^{-1} \otimes I_{n_1}) \cdot \bar{\mathbf{A}} \cdot \text{unfold}(\bar{\mathbf{B}}) \end{aligned}$$

$$\text{unfold}(\bar{\mathbf{C}}) = \bar{\mathbf{A}} \cdot \text{unfold}(\bar{\mathbf{B}}) \implies \bar{\mathbf{C}}^{(i)} = \bar{\mathbf{A}}^{(i)} \bar{\mathbf{B}}^{(i)}$$

Eq. 3.3 and Lemma 3.1 admit an efficient algorithm to compute the t-product using FFTs, as shown in Alg. 3.1.

---

**Algorithm 3.1** Tensor-Tensor Product [9]

---

**Inputs:**  $\mathbf{A} \in \mathbb{R}^{n_1 \times n_2 \times n_3}$ ,  $\mathbf{B} \in \mathbb{R}^{n_2 \times l \times n_3}$

**Output:**  $\mathbf{C} = \mathbf{A} * \mathbf{B} \in \mathbb{R}^{n_1 \times l \times n_3}$

- 1: Compute  $\bar{\mathbf{A}} = \text{fft}(\mathbf{A}, [], 3)$  and  $\bar{\mathbf{B}} = \text{fft}(\mathbf{B}, [], 3)$
- 2: Compute each frontal slice of  $\bar{\mathbf{C}}$  by

$$\bar{\mathbf{C}}^{(i)} = \begin{cases} \bar{\mathbf{A}}^{(i)} \bar{\mathbf{B}}^{(i)}, & i = 1, \dots, \lceil \frac{n_3+1}{2} \rceil \\ \text{conj}(\bar{\mathbf{C}}^{(n_3-i+2)}), & i = \lceil \frac{n_3+1}{2} \rceil + 1, \dots, n_3 \end{cases}$$

- 3: Compute  $\mathbf{C} = \text{ifft}(\bar{\mathbf{C}}, [], 3)$
- 

Like matrix multiplication, the t-product is associative and linear [11]. In the case where  $n_3 = 1$ , it is easy to see that the t-product becomes regular matrix multiplication. Hence, the t-product is just a generalization of matrix multiplication.

DEFINITION 3.3 (Conjugate transpose). [11] The conjugate tranpose of a tensor  $\mathbf{A} \in \mathbb{C}^{n_1 \times n_2 \times n_3}$  is the tensor  $\mathbf{A}^* \in \mathbb{C}^{n_2 \times n_1 \times n_3}$  obtained by conjugate tranposing each frontal slice of  $\mathbf{A}$  and then reversing the order of transposed slices 2 through  $n_3$ .

$$\mathbf{A}^* = \text{fold} \left( \begin{bmatrix} A^{(1)*} \\ A^{(n_3)*} \\ \vdots \\ A^{(2)*} \end{bmatrix} \right)$$

We also denote the conjugate transpose of any matrix or vector as  $A'$  and  $b'$  respectively, and  $A^\dagger$  as the pseudo-inverse of matrix  $A$ .

DEFINITION 3.4 (Identity tensor). [11] The identity tensor  $\mathcal{I}_{nnn_3} \in \mathbb{R}^{n \times n \times n_3}$  is the tensor whose first frontal slice being the  $n \times n$  identity matrix, and all other frontal slices being all zeros. Property:  $\mathcal{A} * \mathcal{I} = \mathcal{I} * \mathcal{A} = \mathcal{A}$

DEFINITION 3.5 (Orthogonal tensor). [11] A tensor  $\mathcal{Q} \in \mathbb{R}^{n \times n \times n_3}$  is orthogonal if it satisfies  $\mathcal{Q}^* * \mathcal{Q} = \mathcal{Q} * \mathcal{Q}^* = \mathcal{I}$ .

DEFINITION 3.6 (F-diagonal tensor). [11] A tensor is called f-diagonal if each of its frontal slices is a diagonal matrix.

### 3.4. T-SVD.

THEOREM 3.7 (T-SVD). [11] Let  $\mathcal{A} \in \mathbb{R}^{n_1 \times n_2 \times n_3}$ . Then it can be factorized as  $\mathcal{A} = \mathcal{U} * \mathcal{S} * \mathcal{V}^*$  where  $\mathcal{U} \in \mathbb{R}^{n_1 \times n_1 \times n_3}$ ,  $\mathcal{V} \in \mathbb{R}^{n_2 \times n_2 \times n_3}$  are orthogonal, and  $\mathcal{S} \in \mathbb{R}^{n_1 \times n_2 \times n_3}$  is an f-diagonal tensor.

We state Theorem 3.7 without proof here and refer the reader to [9] for a detailed proof. The T-SVD can be computed efficiently by Alg. 3.2.

DEFINITION 3.8 (Tensor tubal-rank). [44] For any  $\mathcal{A} \in \mathbb{R}^{n_1 \times n_2 \times n_3}$ , the tensor tubal-rank,  $\text{rank}_t(\mathcal{A})$ , is defined as the number of nonzero singular tubes of  $\mathcal{S}$  from the t-SVD, i.e.,

$$\text{rank}_t(\mathcal{A}) = \#\{i : \mathcal{S}(i, i, :) = \mathbf{0}\}$$

---

#### Algorithm 3.2 T-SVD [9]

---

**Inputs:**  $\mathcal{A} \in \mathbb{R}^{n_1 \times n_2 \times n_3}$   
**Output:** T-SVD components  $\mathcal{U}, \mathcal{S}$ , and  $\mathcal{V}$  of  $\mathcal{A}$ .

- 1: Compute  $\bar{\mathcal{A}} = \text{fft}(\mathcal{A}, [], 3)$
- 2: Compute each frontal slice of  $\bar{\mathcal{U}}, \bar{\mathcal{S}}, \bar{\mathcal{V}}$  by
- 3: **for**  $i = 1, \dots, \lceil \frac{n_3+1}{2} \rceil$  **do**
- 4:    $[\bar{U}^{(i)}, \bar{S}^{(i)}, \bar{V}^{(i)}] = \text{SVD}(\bar{A}^{(i)})$ ;
- 5: **end for**
- 6: **for**  $i = \lceil \frac{n_3+1}{2} \rceil + 1, \dots, n_3$  **do**
- 7:    $\bar{U}^{(i)} = \text{conj}(\bar{U}^{(n_3-i+2)})$ ;
- 8:    $\bar{S}^{(i)} = \text{conj}(\bar{S}^{(n_3-i+2)})$ ;
- 9:    $\bar{V}^{(i)} = \text{conj}(\bar{V}^{(n_3-i+2)})$ ;
- 10: **end for**
- 11: Compute  $\mathcal{U} = \text{ifft}(\bar{\mathcal{U}}, [], 3)$ ,  $\mathcal{S} = \text{ifft}(\bar{\mathcal{S}}, [], 3)$ ,  $\mathcal{V} = \text{ifft}(\bar{\mathcal{V}}, [], 3)$

---

DEFINITION 3.9 (Free Module over the commutative ring). [43] Define  $\mathbb{M}_{n_3}^{n_1}$  to be the set of all 2-D lateral slices of size  $n_1 \times 1 \times n_3$ . Since for any element  $\vec{\mathcal{X}} \in \mathbb{M}_{n_3}^{n_1}$  and coefficient tube  $\vec{v} \in \mathbb{R}^{1 \times 1 \times n_3}$  in the commutative ring  $\mathbb{R}(\mathbb{G}_{n_3})$ , the lateral slice  $\vec{\mathcal{Y}} = \vec{\mathcal{X}} * \vec{v}$  is also an element of  $\mathbb{M}_{n_3}^{n_1}$ , and  $\mathbb{M}_{n_3}^{n_1}$  is closed under tubal-scalar multiplication.

$\mathbb{M}_{n_3}^{n_1}$  is called a free module of dimension  $r < n_1$  over the commutative ring  $\mathbb{R}(\mathbb{G}_{n_3})$  [43]. One can construct a spanning basis  $\{\vec{\mathcal{U}}_1, \vec{\mathcal{U}}_2, \dots, \vec{\mathcal{U}}_r\}$  for this module, and we can uniquely represent any element  $\vec{\mathcal{X}} \in \mathbb{M}_{n_3}^{n_1}$  as a t-linear combination of the spanning basis with some tubal coefficients  $\vec{w}_i$

$$(3.5) \quad \vec{\mathcal{X}} = \sum_{i=1}^r \vec{\mathcal{U}}_i * \vec{w}_i = \mathcal{U} * \vec{\mathcal{W}},$$

and as illustrated in Fig. 1. Above in (3.5),  $\mathcal{U} \in \mathbb{R}^{n_1 \times r \times n_3}$  and  $\vec{\mathcal{W}} \in \mathbb{R}^{r \times 1 \times n_3}$ .

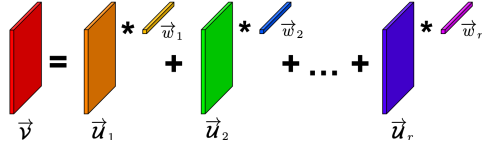


Fig. 1: An element of a free module generated by t-linear combination of spanning basis and coefficients.

**4. Proposed Method.** Much like in matrix PCA where we wish to recover a spanning basis of a lower-dimensional subspace that approximates the vector data samples, we can learn a spanning basis of a lower-dimensional free submodule that approximates the lateral slices of our tensor, where a free submodule is a subset of the free module  $\mathbb{M}_{n_3}^{n_1}$  with a spanning basis of dimension  $d < n_1$  [43].

Given  $n_2$  2-D data samples  $\vec{\mathbf{x}}_1, \dots, \vec{\mathbf{x}}_{n_2}$  of size  $n_1 \times n_3$ , we arrange them as lateral slices to make a 3-D tensor  $\mathbf{X}$  of size  $n_1 \times n_2 \times n_3$  [43]. In most circumstances, the t-SVD method would be used to compute the spanning orthogonal basis (principal components) of this free submodule [21]. For the purposes of this work, we consider the case of 3-D tensor data where each lateral slice arrives sequentially in time and may contain missing entries. Like the work in [43], we wish to compute the spanning low-dimensional free submodule of this multiway streaming data in an online way without computing the t-SVD which may be prohibitive in large data settings.

We can learn the spanning free submodule using stochastic gradient techniques, similar to what the GROUSE algorithm does for matrices with streaming columns. Like GROUSE, we aim to track an  $r$ -dimensional free submodule of  $\mathbb{M}_{n_3}^{n_1}$  that may evolve over time. Let  $\mathbf{U} \in \mathbb{R}^{n_1 \times r \times n_3}$  be an orthonormal tensor whose  $r$  lateral slices span the free submodule of  $\mathbb{M}_{n_3}^{n_1}$ . At every time  $t$ , we observe an incomplete lateral slice  $\vec{\mathbf{v}}_t \in \mathbb{M}_{n_3}^{n_1}$  on the indices  $\Omega_t \subset \{1, \dots, n_1\} \times \{1, \dots, n_3\}$ . We address two cases of missing data: (1) arbitrary missing entries at random and (2) missing tubes at random.

**4.1. Arbitrary Missing Tensor Entries.** In the scenario where the underlying free submodule does not change over time, a natural global optimization problem with squared  $\ell_2$  error loss is given as

$$(4.1) \quad \hat{\mathbf{u}}, \hat{\mathbf{w}} = \underset{\substack{\mathbf{u} \in \mathbb{R}^{n_1 \times r \times n_3} \\ \mathbf{w} \in \mathbb{R}^{r \times n_2 \times n_3}}}{\operatorname{argmin}} \frac{1}{2n_3} \sum_{i,j,k \in \Omega} (\mathbf{v} - \mathbf{u} * \mathbf{w})_{ijk}^2$$

$$\text{s.t. } \mathbf{u}^* * \mathbf{u} = \mathcal{I}_{rrn_3}$$

where  $\mathbf{v} = [\vec{\mathbf{v}}_1 \dots, \vec{\mathbf{v}}_{n_2}]$  is observed on the set of indices  $\Omega \subset \{1, \dots, n_1\} \times \{1, \dots, n_2\} \times \{1, \dots, n_3\}$  and recall that  $\mathcal{I}_{rrn_3}$  is the  $r \times r \times n_3$  tensor identity. Since we have stacked the time slices on the second dimension, let  $n_2 = T$ . We can then rewrite this cost function in terms of each lateral slice  $\vec{\mathbf{v}}_t$  at a time for  $t = 1, 2, \dots, T$  using the Frobenius norm:

$$(4.2) \quad \hat{\mathbf{u}}, \hat{\mathbf{w}} = \underset{\substack{\mathbf{u} \in \mathbb{R}^{n_1 \times r \times n_3} \\ \mathbf{w} \in \mathbb{R}^{r \times T \times n_3}}}{\operatorname{argmin}} \frac{1}{2n_3 T} \sum_{t=1}^T \|\mathcal{A}_{\Omega_t}(\vec{\mathbf{v}}_t - \mathbf{u} * \vec{\mathbf{w}}_t)\|_F^2$$

$$\text{s.t. } \mathbf{u}^* * \mathbf{u} = \mathcal{I}_{rrn_3}$$

where  $\mathcal{A}_{\Omega_t}(\cdot)$  is the linear operator that extracts the observed samples in the set  $\Omega_t$ . From Eq. (4.1), we see it is possible to solve this problem incrementally, like described in [6], in terms of the orthonormal free-submodule  $\mathbf{U}$  and the weights  $\vec{\mathbf{W}}_t \in \mathbb{R}^{n_1 \times 1 \times n_3}$  for all  $t = 1, \dots, T$ .

The problem in (4.1) is an optimization problem on the *tensor Grassmann manifold*, which we define below. [17] gave that the set of 3-D tensors form a smooth embedded manifold  $\mathcal{M}$  of  $\mathbb{R}^n$  that can be realized as a real product manifold of rank- $r$  matrices in the Fourier domain.

LEMMA 4.1 (Cartesian product of manifolds). [1, 17] *Let  $\mathcal{M}_r^i$  be the  $i^{\text{th}}$  smooth manifold of dimension  $r$ . Then the Cartesian product of  $n$  smooth manifolds  $\mathcal{M}$  is itself a smooth manifold.*

$$(4.3) \quad \mathcal{M} = \mathcal{M}_r^1 \times \dots \times \mathcal{M}_r^n$$

THEOREM 4.2 (Tensor Grassmann Manifold). *Let  $\mathbf{U} \in \mathbb{R}^{n_1 \times r \times n_3}$  be an orthonormal tensor and  $\bar{\mathbf{U}} \in \mathbb{C}^{n_1 \times r \times n_3}$  be the result of taking the Fourier transform of each tube in  $\mathbf{U}$ . Let  $\mathcal{G}_r^{(i)}$  be a Grassmann manifold of dimension  $r$  over  $\mathbb{C}^{n_1}$  for the frontal face at index  $i$ . Then from Lemma 4.1,  $\bar{\mathbf{U}}$  lies on the tensor Grassmann manifold  $\mathcal{G}$  that is the set of all free submodules of dimension  $r$  in  $\mathbb{M}_{n_3}^{n_1}$ :*

$$(4.4) \quad \bar{\mathbf{U}} \in \mathcal{G} = \mathcal{G}_r^{(1)} \times \dots \times \mathcal{G}_r^{(n_3)}$$

We note here that  $\mathbf{U}$  is one choice of representation for a point on the tensor Grassmannian where the Fourier transform along its tubes  $\bar{\mathbf{U}}$  has as each frontal face a matrix with orthonormal columns. However, we can equivalently represent this point using an  $n_1 n_3 \times r n_3$  block-diagonal matrix in the Fourier domain, with the frontal faces of  $\bar{\mathbf{U}}$  on the diagonal. We will revisit this representation below.

We minimize the cost function in Eq. (4.1) for each slice  $\vec{\mathbf{V}}_t$  with a stochastic gradient descent procedure. Let  $L_t(\mathbf{U}, \vec{\mathbf{W}}_t) = \frac{1}{2} \|\mathcal{A}_{\Omega_t}(\vec{\mathbf{V}}_t - \mathbf{U} * \vec{\mathbf{W}}_t)\|_F^2$ . Then the objective in Eq. 4.1 is  $\frac{1}{2T} \sum_{t=1}^T L_t(\mathbf{U}, \vec{\mathbf{W}}_t)$ . We will take a gradient step for each  $L_t$  sequentially.

We can rewrite the objective function using the block-circulant matrix definition of the t-product:

$$L_t(\mathbf{U}, \vec{\mathbf{W}}_t) = \frac{1}{2} \|P_{\Omega_t} \cdot \text{unfold}(\vec{\mathbf{V}}_t) - P_{\Omega_t} \cdot (\text{bcirc}(\mathbf{U}) \cdot \text{unfold}(\vec{\mathbf{W}}_t))\|_F^2$$

Here  $P_{\Omega_t}$  is a subsampled identity matrix of size  $|\Omega_t| \times n_1 n_3$ ,  $\text{unfold}(\vec{\mathbf{V}}_t) \in \mathbb{R}^{n_1 n_3 \times 1}$ ,  $\text{bcirc}(\mathbf{U}) \in \mathbb{R}^{n_1 n_3 \times r n_3}$ , and  $\text{unfold}(\vec{\mathbf{W}}_t) \in \mathbb{R}^{r n_3 \times 1}$ . Using block-circulant diagonalization and the fact that  $n_2 = 1$  when processing a single slice, we can rewrite the product  $P_{\Omega_t} \cdot (\text{bcirc}(\mathbf{U}) \cdot \text{unfold}(\vec{\mathbf{W}}_t))$  as

$$\begin{aligned} & P_{\Omega_t} \cdot (F_{n_3}^{-1} \otimes I_{n_1}) \cdot (F_{n_3} \otimes I_{n_1}) \cdot \text{bcirc}(\mathbf{U}) \cdot F_{n_3}^{-1} \cdot F_{n_3} \cdot \text{unfold}(\vec{\mathbf{W}}_t) \\ & = P_{\Omega_t} \cdot (F_{n_3}^{-1} \otimes I_{n_1}) \cdot \bar{U} \cdot \text{unfold}(\vec{\mathbf{W}}_t). \end{aligned}$$

Here we have used the notation from Eq (3.1):

$$\bar{U} = (F_{n_3} \otimes I_{n_1}) \cdot \text{bcirc}(\mathbf{U}) \cdot F_{n_3}^{-1},$$



which is of size  $n_1 n_3 \times r n_3$  and gives us another representation of  $\bar{\mathbf{U}}$ , with the frontal slices of  $\bar{\mathbf{U}}$  on the diagonal, with  $n_3$  blocks of size  $n_1 \times r$ . This representation requires an additional constraint, that the elements not on these diagonal blocks must be zero. We define the convex set  $\mathcal{K}$  to represent these matrices (without any orthogonality constraint). We therefore have the following equivalent form for  $L_t(\mathbf{U}, \vec{\mathbf{W}}_t)$ :

$$(4.5) \quad L_t(\mathbf{U}, \vec{\mathbf{W}}_t) = \frac{1}{2} \|\mathcal{F}_{\Omega_t}(\bar{v} - \bar{U}\bar{w})\|_2^2$$

where  $\bar{v} = \text{unfold}(\bar{V}_t) \in \mathbb{C}^{n_1 n_3}$  and  $\bar{w} = \text{unfold}(\bar{W}_t) \in \mathbb{C}^{r n_3}$  for convenient notation. Finally,  $\mathcal{F}_{\Omega_t} = P_{\Omega_t} \cdot (F_{n_3}^{-1} \otimes I_{n_1}) \in \mathbb{C}^{|\Omega_t| \times n_1 n_3}$  is the subsampled inverse Fourier transform.

This is a nonconvex function because of both the biconvexity between  $\bar{U}$  and  $\bar{w}$  and the orthonormality constraint  $\bar{U}'\bar{U} = I_r$ . One can see the function is separable in each frontal slice in the Fourier domain. Our stochastic gradient procedure will fix  $\bar{U}$  and then minimize  $L_t(\mathbf{U}, \vec{\mathbf{W}}_t)$  with respect to  $\bar{w}$  (equivalently  $\bar{W}_t$ ); then we fix  $\bar{w}$  and take a step in the negative gradient direction of  $L_t(\mathbf{U}, \vec{\mathbf{W}}_t)$  with respect to  $\bar{U}$  (equiv.  $\mathbf{U}$ ). Note that  $\bar{U}^{(i)} \in \mathcal{G}(r, n_1)$ ,  $\forall i = 1, \dots, n_3$ , where  $\mathcal{G}(r, n_1)$  denotes the complex Grassmannian—the set of all subspaces of dimension  $r$  in  $\mathbb{C}^{n_1}$ . Updating the free submodule  $\bar{U}$  involves a projected gradient descent step onto the set of block-diagonal matrices in the Fourier domain followed by a geodesic step along each complex Grassmann manifold in the product of manifolds.

**4.1.1. Updating the weights  $\vec{\mathbf{W}}_t$ .** First we optimize for  $\bar{w}$  holding  $\bar{U}$  fixed by solving

$$(4.6) \quad \bar{w} = \underset{\bar{a} \in \mathbb{C}^{r n_3}}{\text{argmin}} \frac{1}{2} \|\mathcal{F}_{\Omega_t}(\bar{v} - \bar{U}\bar{a})\|_2^2.$$

Solving for the optimal  $\bar{w}$  in a closed form involves forming and inverting a large matrix of size  $r n_3 \times r n_3$ . Instead, we use conjugate gradient descent (CGD) to estimate  $\bar{w}$ . This problem is easily and efficiently solved with CGD since the problem in Eq. (4.6) is convex and quadratic in  $\bar{a}$  with  $\bar{U}$  fixed. Furthermore, we can easily compute the matrix-vector products  $\bar{U}'\mathcal{F}'_{\Omega_t}\mathcal{F}_{\Omega_t}\bar{U}x$  for some vector  $x \in \mathbb{C}^{r n_3}$  using fast Fourier transforms, separable matrix-vector products in each slice (from the block diagonal structure of  $\bar{U}$ ), and zero-padding.

As the number of missing entries increases, the matrix  $\mathcal{F}_{\Omega_t}\bar{U}$  in the least squares problem of Eq. (4.6) becomes more poorly conditioned. Because the convergence rate of conjugate gradient descent is dependent on the condition number of this matrix,  $\kappa(\mathcal{F}_{\Omega_t}\bar{U})$ , the algorithm will require more iterations to solve the problem to within some  $\epsilon > 0$  accuracy. However, as noted above, it is impractical to form and store this large matrix, much less compute its SVD to find  $\kappa$ , but we do know the sampling rate. Below we prove the upper bound on the number of CGD iterations as a function of the number of samples. The following lemma utilizes the notion of coherence of an  $m \times r$  subspace basis  $U$ , defined as  $\mu(U) = \max_{1 \leq i \leq m} \|\mathbf{P}_U e_i\|_2^2$ , where  $\mathbf{P}_U$  is the orthogonal projection onto  $U$  and  $e_i$  is the  $i^{\text{th}}$  standard basis vector [8].

First we state the result from Lemma 8.3.3 of [3]:

**LEMMA 4.3.** [3] *Let  $U$  be an  $m \times r$  matrix with orthonormal columns, and let  $S$  be a random subsampling operator that samples  $|\Omega| \leq m$  rows from  $U$  uniformly. Let  $C$  be a universal constant, and  $\delta \in [0, 1]$ . Then with probability  $1 - \delta$*

$$(4.7) \quad \mathbb{E}\{\|I_\tau - \frac{m}{|\Omega|} U' S' S U\|\} \leq C \sqrt{m\mu(U) \log(|\Omega|)/|\Omega|} := \tau, \text{ and}$$

$$(4.8) \quad \kappa(SU) \leq \sqrt{\frac{1 + \delta^{-1}\tau}{1 - \delta^{-1}\tau}}.$$

Using the results of Lemma 4.3, we can upper bound on the number of CGD iterations in terms of  $\mu(\mathcal{F}_{\Omega_t} \bar{U})$ :

**THEOREM 4.4.** *Let  $P_{\Omega_t}$  sample  $|\Omega_t|$  rows from  $\mathcal{F}_{\Omega_t} \bar{U}$  uniformly at random. Let  $\epsilon > 0$ ,  $\delta > 0$  and  $C_1$  be a universal constant. Then with probability  $1 - \delta$ , the maximum number of conjugate gradient descent iterations,  $K$ , required to solve (4.6) to within  $\epsilon$ -precision is upper bounded as:*

$$(4.9) \quad K \leq \frac{1}{2} \sqrt{\frac{1 + \delta^{-1}\tau}{1 - \delta^{-1}\tau}} \log(2/\epsilon), \text{ where } \tau := C_1 \sqrt{n_1 n_3 \mu(\mathcal{F}_{\Omega_t} \bar{U}) \log(|\Omega|)/(|\Omega|)}.$$

Computing the coherence of  $\mathcal{F}_{\Omega_t} \bar{U}$  may be burdensome in practice. If we could bound the coherence of our iterates, we would be able to plug the bound into the above theorem. However, it is difficult to guarantee bounds of that sort without strong assumptions on the data. Starting from a random i.i.d. Gaussian initialization, empirical evidence generally supports the assumption that the coherence of the subspace doesn't exceed a constant multiple of the initial coherence. With this assumption, we may refine our upper bound using Lemma 2.2 from [8], given now for completeness. We show empirically in Section 4 that this bound on the coherence gives a reasonable upper bound for the number of CGD iterations in practice.

**LEMMA 4.5.** [8] *Let  $U$  be a subspace of  $\mathbb{R}^m$  of dimension  $r$ , and  $\mathbf{P}_U$  be the orthogonal projection onto  $U$ . Set  $\bar{r} = \max\{r, \log(m)\}$ . Then there exist constants  $C_2$  and  $c$  such that the coherence of  $U$ , denoted  $\mu(U)$ ,*

$$(4.10) \quad \mu(U) = \max_i \|\mathbf{P}_U e_i\|^2 \leq C_2 \bar{r}/m$$

with probability  $1 - cm^{-3} \log(m)$ .

In the above Lemma, the probability is with respect to entries of  $U$  here, which are assumed to be i.i.d. Gaussian. Under this somewhat strong assumption that the iterates' coherence remains bounded,  $\tau \leq C_1 \sqrt{C_2 \max\{r, \log(n_1 n_3)\} \log(|\Omega|)/(|\Omega|)}$  with probability  $1 - \delta c(n_1 n_3)^{-3} \log(n_1 n_3)$ , where  $C_2$  and  $c$  are constants and we assume the condition number and coherence bounds are independent.

**4.1.2. Updating  $\mathcal{U}$ .** Next we perform a step of projected gradient descent on the Grassmannian in each slice in the complex domain while holding  $\bar{w}$  fixed. We compute the gradient of the objective function  $L_t$  projected onto the convex set  $\mathcal{K}$ , and then follow this gradient along a short geodesic curve on the Grassmannian [4]. First, using matrix derivatives [33], we find the partial derivatives of  $L_t$  with respect to the components of  $\bar{U}$ :

$$(4.11) \quad \frac{\partial L_t}{\partial \bar{U}} = -\mathcal{F}'_{\Omega_t} \mathcal{F}_{\Omega_t} (\bar{v} - \bar{U} \bar{w}) \bar{w}' = -\mathcal{F}'_{\Omega_t} \mathcal{F}_{\Omega_t} \bar{r} \bar{w}'$$

Using the work in [12], the projected gradient on the Grassmannian in Fourier space is given by

$$(4.12) \quad \nabla L_t = \mathcal{P}_{\mathcal{K}} \left( (I - \bar{U}\bar{U}') \frac{\partial L_t}{\partial \bar{U}} \right),$$

where  $\mathcal{P}_{\mathcal{K}}(\cdot)$  projects the gradient onto the closest point in the set  $\mathcal{K}$  which sets the non-block-diagonal entries of the gradient to zero. The gradient of the objective on the Grassmannian then has the form

$$(4.13) \quad \nabla L_t = \begin{bmatrix} -\bar{\rho}^{(1)}\bar{w}^{(1)'} & & 0 \\ & \ddots & \\ 0 & & -\bar{\rho}^{(n_3)}\bar{w}^{(n_3)'} \end{bmatrix} \in \mathbb{C}^{n_1 n_3 \times r n_3}$$

where

$$(4.14) \quad \bar{\rho}^{(i)} = \left( I - \bar{U}^{(i)}\bar{U}^{(i)'} \right) \bar{r}_{\Omega_t}^{(i)}$$

$$(4.15) \quad \bar{r}_{\Omega_t} = \mathcal{F}'_{\Omega_t} \mathcal{F}_{\Omega_t} \bar{r} = \text{unfold}(\text{fft}(\Delta_{\Omega_t}(\vec{\mathcal{R}}), [], 3)).$$

Here,  $\vec{\mathcal{R}} = \vec{\mathcal{Y}} - \mathbf{u} * \vec{\mathcal{W}}$  and  $\Delta_{\Omega_t}(\cdot)$  imputes zeros on the unobserved tensor entries.

A gradient step along the geodesic with tangent vector  $-\nabla L_t$  is given by Equation (2.65) in [12] and is a function of the singular values and vectors of  $\nabla L_t$  [4]. We can express the SVD of  $\nabla L_t$  as a product of block-diagonal matrices where each element on the diagonal of  $\nabla L_t$  is itself a rank-one SVD:

$$(4.16) \quad \nabla L_t^{(i)} = \begin{cases} U^{(i)} \Sigma^{(i)} V^{(i)'}, & i = 1, \dots, \lceil \frac{n_3+1}{2} \rceil \\ \text{conj}(\nabla L_t^{(i)}), & i = \lceil \frac{n_3+1}{2} \rceil + 1, \dots, n_3 \end{cases}$$

$$U^{(i)} = \left[ \frac{-\bar{\rho}^{(i)}}{\|\bar{\rho}^{(i)}\|}, x_2^{(i)}, \dots, x_r^{(i)} \right]$$

$$\Sigma^{(i)} = \text{diag}\{\bar{\sigma}^{(i)}, 0, \dots, 0\}$$

$$V^{(i)'} = \left[ \frac{\bar{w}^{(i)}}{\|\bar{w}^{(i)}\|}, y_2^{(i)}, \dots, y_r^{(i)} \right]',$$

where  $\bar{\sigma}^{(i)} := 2 \cdot \|\bar{\rho}^{(i)}\| \cdot \|\bar{w}^{(i)'}\|$ . Above,  $\bar{\rho}^{(i)}/\|\bar{\rho}^{(i)}\|$  and  $\bar{w}^{(i)'}/\|\bar{w}^{(i)}\|$  indicate that each vector slice in Fourier space is normalized by its  $\ell_2$  norm. The orthonormal set of vectors  $x_2^{(i)}, \dots, x_r^{(i)}$  and  $y_2^{(i)}, \dots, y_r^{(i)}$  are orthogonal to  $\bar{\rho}^{(i)}$  and  $\bar{w}^{(i)}$  respectively.

From [12], a step of length  $\eta > 0$  in the direction  $-\nabla L_t$  is given by

$$(4.17)$$

$$\bar{\mathbf{u}}_{t+1} = \bar{\mathbf{u}}_t + \bar{\mathbf{H}}$$

$$\bar{H}^{(i)} = \begin{cases} \left( \sin(\bar{\sigma}^{(i)}\eta) \frac{\bar{\rho}^{(i)}}{\|\bar{\rho}^{(i)}\|} + (\cos(\bar{\sigma}^{(i)}\eta) - 1) \frac{\bar{\rho}^{(i)}}{\|\bar{\rho}^{(i)}\|} \right) \frac{\bar{w}^{(i)'}}{\|\bar{w}^{(i)}\|}, & i = 1, \dots, \lceil \frac{n_3+1}{2} \rceil \\ \text{conj}(\bar{H}^{(i)}), & i = \lceil \frac{n_3+1}{2} \rceil + 1, \dots, n_3 \end{cases}$$

where  $\bar{\rho}^{(i)} = \bar{U}^{(i)}\bar{w}^{(i)}$ .

Following from the convergence analysis of GROUSE in [40], we use a greedy step size  $\eta = \arctan(\|\bar{\rho}^{(i)}\|/\|\bar{w}^{(i)}\|)$  above for each slice  $\bar{H}^{(i)}$ .

Using Lemma 3.1, we can save significant time by only computing the matrix-vector multiplications on half of the frontal slices in the Fourier domain and using the complex conjugate to find the others.

The preceding updates give an efficient algorithm we call TOUCAN (Tensor rank-One Update on the Complex grassmanniAN) for computing each variable in the Fourier domain with simple, efficient linear algebra operations and fast Fourier transforms. TOUCAN is numerically stable by maintaining orthonormality on the tensor Grassmannian and is constant in memory use, scaling linearly with the number of observed data samples instead of in polynomial-time like batch t-SVD methods. TOUCAN is summarized in Algorithm 4.1.

---

**Algorithm 4.1** Tensor rank-One Update on the Complex grassmanniAN (TOUCAN): Arbitrary Missing Tensor Entries

---

**Require:** A series of lateral slices  $\vec{\mathbf{v}}_t \in \mathbb{R}^{n_1 \times 1 \times n_3}$ ,  $\forall i = 1, \dots, T$  observed on the indices in  $\Omega_t$ ; Fourier transformed orthonormal tensor  $\vec{\mathbf{u}}_0 \in \mathbb{C}^{n_1 \times r \times n_3}$ .

- 1: **for**  $t = 1$  to  $T$  **do**
  - 2:   Compute  $\vec{\mathbf{v}}_t = \text{ifft}(\mathbf{v}_t, [], 3)$
  - 3:   Estimate weights  $\vec{\mathbf{w}}_t$  by solving Eq. (4.6) with CGD.
  - 4:   Predict full vector:  $\vec{\mathbf{p}} = \vec{\mathbf{u}}_t \vec{\mathbf{w}}_t$
  - 5:   Transform:  $\vec{\mathbf{p}} = \text{ifft}(\vec{\mathbf{p}}, [], 3)$
  - 6:   Compute residual:  $\vec{\mathbf{r}} = \vec{\mathbf{v}}_t - \vec{\mathbf{p}}$
  - 7:   Compute gradient terms from Eqs. (4.15) and (4.14).
  - 8:   Compute  $\vec{\mathbf{h}}$  in Eq. (4.17)
  - 9:   Update subspace:  $\vec{\mathbf{u}}_{t+1} = \vec{\mathbf{u}}_t + \vec{\mathbf{h}}$
  - 10:   Transform:  $\vec{\mathbf{u}}_{t+1} = \text{ifft}(\vec{\mathbf{u}}_{t+1}, [], 3)$
  - 11:   Transform:  $\vec{\mathbf{w}}_t = \text{ifft}(\mathbf{w}_t, [], 3)$
  - 12: **end for**
  - 13: **return**  $\vec{\mathbf{u}}_{t+1}, \vec{\mathbf{w}}_t$ ,  $\forall t = 1, \dots, T$
- 

**4.1.3. Memory and computational analysis.** TOUCAN needs to only store an orthonormal tensor  $\vec{\mathbf{u}}_t \in \mathbb{R}^{n_1 \times r \times n_3}$ , the weights  $\vec{\mathbf{w}}_t \in \mathbb{R}^{r \times 1 \times n_3}$  at each time instance  $t = 1, \dots, T$ , requiring  $n_1 r n_3 + r n_3$  memory elements per time instance. This is far fewer than storing the entire tensor in memory which would require  $n_1 T n_3$  memory elements, especially when any of the dimensions is very large.

Implemented efficiently, the main loop of our algorithm requires 4 fast inverse Fourier transforms and one fast Fourier Transform. The CGD update takes  $O(K(Nn_1r + n_1n_3 \log(n_3)))$  flops where  $N = \lceil (n_3 + 1)/2 \rceil$  and  $K$  is the number of CGD iterations. Computing  $\vec{\mathbf{r}}$  takes  $O(Nn_1r + n_1n_3 \log(n_3) + n_1n_3)$  flops. The update in Eq. 4.15 takes  $n_1n_3 \log(n_3)$  flops, and Eq. 4.14 takes  $O(Nn_1r)$  flops. Computing the subspace update requires  $O(Nn_1r)$  flops. In total, one iteration of TOUCAN takes  $O(Nrn_1 + n_1n_3 + K(Nrn_1 + n_1n_3 \log(n_3)))$  flops.

**4.2. Missing Tensor Tubes.** In real applications, entire tensor tubes may be missing. For example, in MRI data collection, due to storage and computation requirements, it is often efficient to only sample entire rows or columns of spatial-frequency space. In our framework, recovering an entire tensor tube is actually easier than imputing individual random missing entries, and it admits an even more efficient algorithm.

Again, let  $\mathbf{v} = [\vec{\mathbf{v}}_1 \dots, \vec{\mathbf{v}}_T] \in \mathbb{R}^{n_1 \times T \times n_3}$  be a set of lateral slices for each time

instance. At every time  $t$ , we observe an incomplete lateral slice  $\mathbf{V}_t \in \mathbb{M}_{n_3}^{n_1}$  on the indices  $\Omega_t \subset \{1, \dots, n_1\}$  where not all tubes of the slice are observed. Denote  $\mathcal{P}_{\Omega_t} \in \mathbb{R}^{|\Omega_t| \times n_1 \times n_3}$  as the tensor that selects the coordinate axes of  $\mathbb{R}^{n_1}$  indexed by  $\Omega_t$ .  $\mathcal{P}_{\Omega_t}$  is a tensor whose first frontal slice is a subsampled identity matrix on the rows indexed by  $\Omega_t$ ; all other frontal slices are zeros. We then observe the lateral slice  $\mathcal{P}_{\Omega_t} * \vec{\mathbf{V}}_t$  at time  $t$ . Let  $\mathbf{U}_{\Omega_t}$  denote the subtensor of  $\mathbf{U}$  consisting of the tubes indexed by  $\Omega_t$ , and  $\mathbf{V}_{\Omega_t} = \mathcal{P}_{\Omega_t} * \vec{\mathbf{V}}_t$  denote a lateral slice in  $\mathbb{R}^{|\Omega_t| \times 1 \times n_3}$  observed on the tubes indexed by  $\Omega_t$ . It can be shown that the objective function can be rewritten as

$$(4.18) \quad \hat{\mathbf{U}}, \hat{\mathbf{W}} = \underset{\mathbf{U} \in \mathbb{R}^{n_1 \times r \times n_3}, \mathbf{W} \in \mathbb{R}^{r \times T \times n_3}}{\operatorname{argmin}} \frac{1}{2n_3 T} \sum_{i=1}^T \|\vec{\mathbf{V}}_{\Omega_t} - \mathbf{U}_{\Omega_t} * \vec{\mathbf{W}}_t\|_F^2$$

s.t.  $\mathbf{U}^* * \mathbf{U} = \mathcal{I}_{rrn_3}$

In the Fourier domain,  $L_t$  becomes

$$(4.19) \quad L_t(\mathbf{U}, \vec{\mathbf{W}}_t) = \frac{1}{2n_3} \|\bar{\mathbf{V}}_{\Omega_t} - \bar{\mathbf{U}}_{\Omega_t} \bar{\mathbf{W}}_t\|_F^2$$

The notation  $\bar{\mathbf{U}}_{\Omega_t} \in \mathbb{C}^{|\Omega_t| n_3 \times r n_3}$  denotes the block-diagonal matrix of  $\bar{\mathbf{U}}$  consisting of the rows indexed by  $\Omega_t$ . Similarly,  $\bar{\mathbf{V}}_{\Omega_t}$  is a block-diagonal matrix in  $\mathbb{R}^{|\Omega_t| n_3 \times n_3}$  observed on the rows indexed by  $\Omega_t$ . The problem is block-diagonal, and as the work in [17] showed, it is separable in each frontal slice in the Fourier domain, so each problem is a Grassmann manifold optimization problem. The algorithm is similar to that in Alg. 4.1, except  $\vec{\mathbf{W}}$  can be solved exactly in closed form using pseudo-inverses in the Fourier domain, and  $\bar{\rho}^{(i)}$  is replaced by  $\bar{r}^{(i)}$  in Eq. 4.17. Likewise, our step size is  $\eta = \arctan(\|\bar{r}^{(i)}\| / \|\bar{w}^{(i)}\|)$ .

We give the full algorithm in Algorithm 4.2.

---

**Algorithm 4.2** Tensor rank-One Update on the Complex grassmannian (TOUCAN): Missing Tensor Tubes

---

**Require:** A series of lateral slices  $\vec{\mathbf{V}}_t \in \mathbb{R}^{n_1 \times 1 \times n_3}$ ,  $\forall i = 1, \dots, T$  observed on the indices in  $\Omega_t$ ; Fourier transformed orthonormal tensor  $\bar{\mathbf{U}}_0 \in \mathbb{C}^{n_1 \times 1 \times n_3}$ .

- 1: **for**  $t = 1$  to  $T$  **do**
  - 2:   Compute  $\vec{\mathbf{V}}_t = \operatorname{ifft}(\mathbf{V}_t, \square, 3)$
  - 3:   Estimate weights:  $\bar{\mathbf{W}}_t^{(i)} = \bar{\mathbf{U}}_{\Omega_t}^{(i)\dagger} \bar{\mathbf{V}}_{\Omega_t}^{(i)}$
  - 4:   Predict full vector:  $\bar{\mathbf{P}} = \bar{\mathbf{U}}_t \bar{\mathbf{W}}_t$
  - 5:   Transform:  $\vec{\mathbf{P}} = \operatorname{ifft}(\bar{\mathbf{P}}, \square, 3)$
  - 6:   Compute residual:  $\vec{\mathbf{R}} = \Delta_{\Omega_t}(\vec{\mathbf{V}}_t - \vec{\mathbf{P}})$
  - 7:   Compute  $\bar{\mathbf{H}}$ .
  - 8:   Update subspace:  $\bar{\mathbf{U}}_{t+1} = \bar{\mathbf{U}}_t + \bar{\mathbf{H}}$
  - 9:   Transform:  $\mathbf{U}_{t+1} = \operatorname{ifft}(\bar{\mathbf{U}}_{t+1}, \square, 3)$
  - 10:   Transform:  $\vec{\mathbf{W}}_t = \operatorname{ifft}(\mathbf{W}_t, \square, 3)$
  - 11: **end for**
  - 12: **return**  $\mathbf{U}_{t+1}, \vec{\mathbf{W}}_t$ ,  $\forall t = 1, \dots, T$
- 

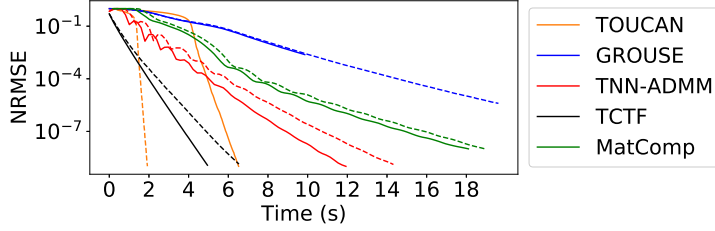
## 5. Experimental Results.

### 5.1. Synthetic data experiments.

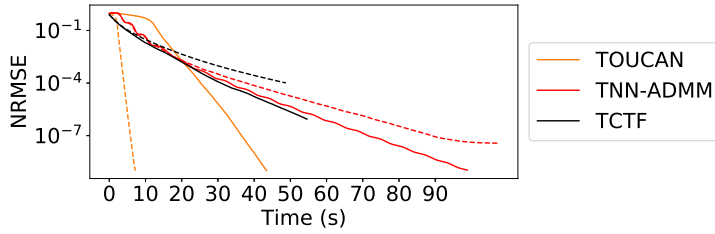
**5.1.1. Incremental Tensor Completion.** We first verify the validity and efficiency of TOUCAN in recovering large-scale missing tensor data synthetically generated from isotropic Gaussian distributions with low-tubal-rank. We compute the t-product of two low-tubal-rank tensors to yield a tensor of size  $n_1 \times n_2 \times n_3$  with tubal-rank  $r = 3$ . We sample a percentage of tensor entries/tubes randomly according to a Bernoulli distribution. TOUCAN observes one lateral slice at each time instant, solves the inner CGD step to within a set tolerance ( $1e - 9$ ), and is allowed to process over the entire batch more than once until the desired termination tolerance. We compare against t-SVD batch tensor completion algorithms (with improved computational efficiency using conjugate symmetry); one uses the tensor nuclear norm and performs ADMM in its optimization (TNN-ADMM) [41], and the other factorizes the tensor as the product of two low-tubal-rank tensors under the t-product (TCTF) [44]. We also compare to standard matrix PCA algorithms by matricizing the tensor and computing batch matrix completion [7] and GROUSE [4] on each column of the matricized tensor. We plot the normalized root-mean-squared error (NRMSE) of the recovered tensor to the true tensor by elapsed wall clock time in seconds in Fig. 2(a) and 2(b), terminating each algorithm if its completed tensor  $\hat{\mathcal{X}}$  satisfies  $\|\hat{\mathcal{X}} - \mathcal{X}\|_F / \|\mathcal{X}\|_F \leq 1e - 9$ . TOUCAN is competitive with state-of-the-art batch method Tensor Factorization (TCTF) [44] in the case of random entry sampling, and TOUCAN’s efficient tubal-sampling implementation vastly outperforms the other algorithms while using only 0.6% of the memory compared to storing the entire tensor.

We note that CP completion algorithms fail completely in our experiments on t-SVD generated data. We conjecture it is because the t-SVD is an oriented operator; since CP algorithms seek a decomposition independent of tensor orientation, a CP decomposition might not be obtainable. Thus we omit them from the t-SVD synthetic experiments results. However, we compared TOUCAN to other tensor completion methods, including CP methods OLSTEC [20] and TeCPSGD [29], on CP-generated synthetic data. Because the t-SVD decomposition can be written as a CP decomposition and the fact that the CP rank is equal to the tubal-rank [11], the t-SVD tensor algorithms should be able to impute missing entries from a low-rank CP model. We generate three-way CP synthetic data of CP rank  $r$  from three factor matrices of sizes  $n_1 \times r$ ,  $n_2 \times r$ , and  $n_3 \times r$  with i.i.d. Gaussian entries. Our results are shown in Fig. 3. TOUCAN is able to impute missing tensor entries for CP models with very low rank but begins to fail with any higher choice of rank, in contrast to the batch t-SVD algorithms which still succeed. Taking the t-SVD of the CP-generated data and inspecting the first-slice singular values shows a larger singular value gap between the first and last nonzero singular values, which is likely the reason TOUCAN’s free submodule tracking ability becomes poor, much like GROUSE’s in poorly conditioned matrix data.

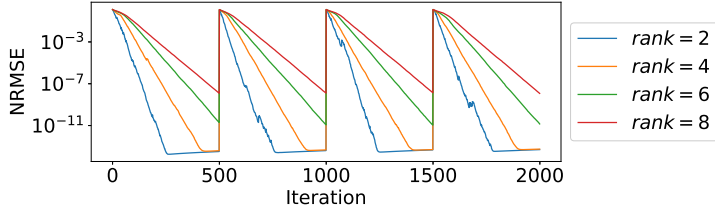
**5.1.2. Dynamic FSM Tracking.** We demonstrate TOUCAN’s ability to track a dynamically changing free submodule (FSM) from streaming multiway data with missing entries. We generate a random orthonormal basis  $\mathbf{U}$  for various tubal-ranks from an i.i.d. Gaussian distribution and draw 2-D lateral slices by t-product with i.i.d. Gaussian weights. We sample 70% of the entries/tubes at random. At each iteration, for TOUCAN’s estimate  $\hat{\mathbf{U}}$ , we measure  $\|\hat{\mathbf{U}} * \hat{\mathbf{U}}^* - \mathbf{U} * \mathbf{U}^*\|_F / \|\mathbf{U} * \mathbf{U}^*\|_F$ . We simulate abrupt FSM changes by randomly reinitializing the underlying FSM every 500 slices. The simulation results in Fig. 2(c) show TOUCAN’s ability to reliably re-estimate each new FSM.



(a)  $n_1 = 200, n_2 = 500, n_3 = 20, r = 3$ . 50% missing t-SVD generated data. Solid lines are experiments with uniformly random samples, and dashed lines are experiments with uniformly sampled tubes.



(b)  $n_1 = 200, n_2 = 500, n_3 = 25, r = 5$ . 80% missing t-SVD generated data. Solid lines are experiments with uniformly random samples, and dashed lines are experiments with uniformly sampled tubes.



(c) TOUCAN tracking dynamic FSMs of different tubal-ranks under random sampling for t-SVD generated data. The low rank model changes every 500 time steps. Here,  $n_1 = 50$  and  $n_3 = 10$ .

Fig. 2: t-SVD synthetic experiments.

**5.1.3. Empirical results for CGD iteration bound.** We demonstrate that TOUCAN empirically obeys our derived upper bound from Theorem 4.4 (or Equation 4.10). We generate a small problem of synthetic data of size  $n_1 = 50, n_2 = 200, n_3 = 20$  with tubal-rank 5 from a synthetic FSM  $\mathbf{U}_0 \in \mathbb{R}^{n_1 \times r \times n_3}$ . We construct the full matrix  $\mathcal{F}_{\Omega_t} \bar{U}_0$  and compute the average  $\kappa(\mathcal{F}_{\Omega_t} \bar{U}_0)^2$  for 20 random sampling patterns for each sampling rate and use this to compute the CGD sample bound. We also plot our bound derived in Theorem 4.4. We let TOUCAN process the data and record the average number of CGD iterations per algorithm iteration. We plot the results in Fig. 4 along with the recovered tensor NRMSE; the horizontal axis is  $dof/|\Omega|$

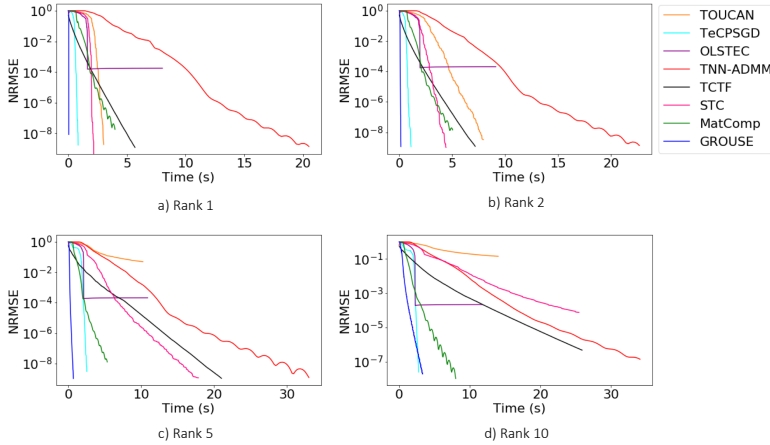


Fig. 3: CP-generated synthetic experiments.  $n_1 = n_2 = n_3 = 100$ .

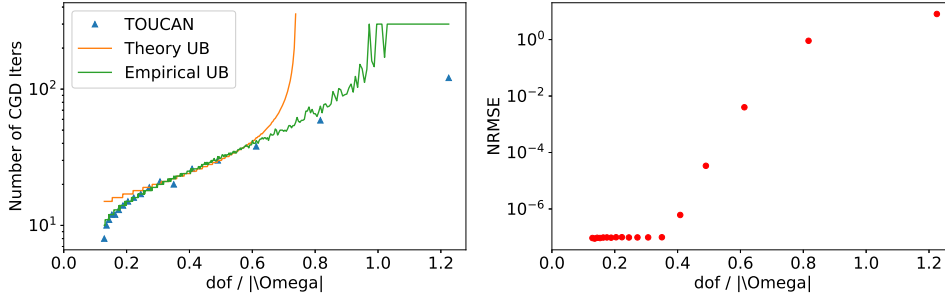


Fig. 4: Number of average conjugate gradient iterations per TOUCAN iteration with varying sampling rates. We compare to the empirical bound based on the computed condition number and the bound in Theorem 4.4. The right plot shows the recovery error by sampling rate.

where  $dof = n_3r((n_1 + n_2) - r)$  is the degrees of freedom of the set of tubal-rank  $r$  tensors and  $|\Omega|$  again is the number of observed samples. We do not plot the empirical number of CGD iterations above 300. We observe two regions of interest—one where the number of CGD iterations is near-linear as a function of the sampling rate, and one where the number of iterations exponentially increases as the data becomes highly undersampled. It is in this transition we see TOUCAN’s completion ability begins to fail. While our bound is fairly tight in the linear region, it is quite loose in the highly-undersampled regime.

## 5.2. Real data experiments.

**5.2.1. Application to Gas Measurements Tensor.** We demonstrate TOUCAN’s ability to track a dynamically changing free submodule from streaming 2-D lateral slice data with missing entries in chemo-sensing data collected by Vergara et al. [37]. The dataset consists of measurements as a gas is blown over an array of conductometric metal-oxide sensors in a wind tunnel [23]. The data is made up of 6 arrays each with 72 sensors, 260 seconds of data points collected at  $\sim 100$  Hz, and 300



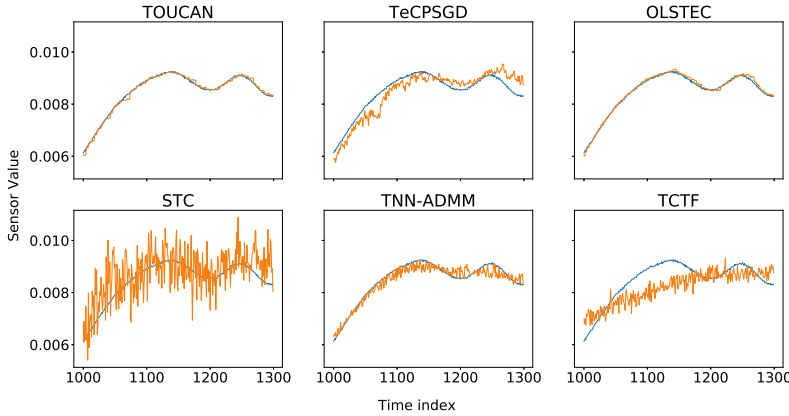


Fig. 5: The blue curve represents the true signal value for sensor 34 in experiment 100, and orange represents each algorithm’s recovered trace.

experiments for each of 11 gases. The sensor values vary in time as a gas permeates throughout a wind tunnel and then dissipates [23]. We chose to fix the array and gas, using the fourth sensor array and Toulene gas for our experiments, downsample to 10 Hz, and remove sensor 33 (out of 72) and time samples 1103 and 2012, which seemed to have erratic measurements. resulting in a tensor of size  $300 \times 2600 \times 71$ . Before running TOUCAN, we demean the columns of each time slice– a column referring to 300 experiment samples per sensor– and normalize each time slice by its Frobenius norm. After computing one t-SVD over the entire data, we found the data to have approximate tubal-rank 7, and approximate tubal-rank 1 over small windows of time. We subsample only 25% of the data and track a 1-dimensional free submodule with TOUCAN.

The online algorithms process each time slice sequentially, observing a  $300 \times 71$  matrix of experiments versus sensor channels. TOUCAN updates its estimate of  $\vec{u}_t$ , and weights  $\vec{w}_t$ . The lateral slice with imputed values is then  $\vec{v}_t = \vec{u}_t * \vec{w}_t$ . For competing algorithms, we tuned parameters by hand with a grid search to find the best performance. We set  $\lambda = 1e - 4$  and the initial step size to be  $1e4$  for TeCPSGD, and we set  $\lambda = 0.9$  and  $\mu = 1e - 8$  for OLSTEC. STC learns subspaces of ranks 20, 20, and 1 for the three unfoldings. We set TCTF to learn a tubal-rank 7 factorization, and we set the ADMM algorithm penalty  $\rho = 1.5$  for TNN-ADMM. The batch algorithms are allowed to compute until the difference NRMSE between iterates is less than  $1e - 4$ . For visualization, we plot the predicted sensor curves of each algorithm in Fig. 5 for sensor number 34 in experiment 100. We also compare the NRMSE of each recovered 2D slice to the true data at each time instance for the algorithms and display the results in Fig. 6, which shows TOUCAN tracking the sensor readings with comparable error to OLSTEC. We also give the total computation time for each algorithm in table 1 and show the significant speedup TOUCAN attains over the baseline algorithms, particularly the batch algorithms that are computationally prohibitive with large tensor data.

**5.2.2. Streaming dynamic MRI reconstruction.** Magnetic resonance imaging (MRI) collects a high-dimensional tensor that is often undersampled due to com-

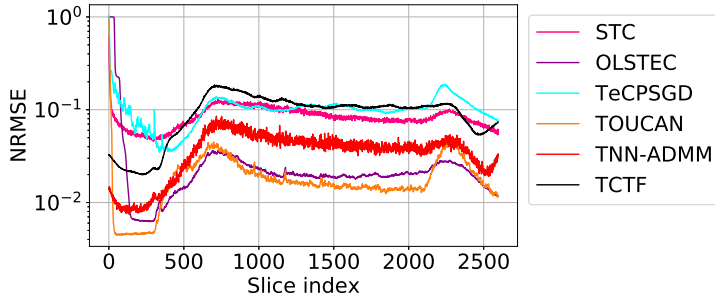


Fig. 6: NRMSE of each recovered time slice for Toluene gas dataset from 25% samples.

Algorithm	Time (s)
TOUCAN	27.77
TeCPSGD	45.29
OLSTEC	382.90
TNN-ADMM	844.26
TCTF	519.53
STC	34.82

Table 1: Total wall clock time of each algorithm.

putational limitations exacerbated by large volumetric and dynamic acquisitions. One successful solution to image reconstruction from limited sampling is low-rank tensor completion [5, 29]. A t-SVD factorization of the spatial frequency-by-time (or  $k$ - $t$  space) tensor shows low-tubal-rank structure in the real and complex components [5], and t-SVD algorithms have been shown to be proficient at completing the  $k$ - $t$  space tensor for image reconstruction. MRI data can also contain significant motion content and time-varying dynamics such as breathing motion. We employ TOUCAN’s ability to track streaming time-dynamic multiway data to recover the  $k$ - $t$  space tensor.

We test TOUCAN against the batch t-SVD algorithms, the two online CP algorithms, and STC to recover undersampled MRI data. We test the completion abilities of each algorithm on two datasets with both uniformly random entry sampling and tube sampling along the  $k_y$  direction. The first dataset is a 2D resting state fMRI capturing brain activities due to BOLD signal fluctuations obtained by Amos Cao in BME at the University of Michigan; it contains  $100 \times 100$  spatial frequencies over 300 time points ( $k_x = k_y = 100$  and  $k_t = 300$ ) to give a tensor in  $\mathbb{C}^{k_x \times k_t \times k_y}$ . The data is fairly static with subtle visual fluctuations, so its CP and tubal-ranks are very low. The second is an invivo myocardial perfusion dataset data from [25] where  $k_x = 190, k_y = 90$  and  $k_t = 70$ . This data contains many dynamic motions such as heartbeats, breathing motion, and image intensity changes.

TOUCAN processes both datasets with the  $k$ -space rows oriented along the third tensor mode ( $k_y = n_3$ ). We allow the online methods one pass over each dataset in a streaming way. TOUCAN learns free submodules of tubal-ranks 1 and 5 respectively, and we set the ranks  $r_1 = r_2 = 25, r_3 = 5$  for STC. STC cannot handle tube-sampled data since an entire column of one of the tensor unfoldings will be missing, so we only test it in the case where arbitrarily random entries are missing. We use the source code from [20] for our implementations of OLSTEC and TeCPSGD. Each algorithm learns a rank-50 CP decomposition; for the brain dataset, we set  $\lambda = 0.8$  and  $\mu = 0.001$  for OLSTEC, and  $\lambda = 0.001$  and the initial step size to be 0.01 for

	Sample %	NRMSE		SSIM		Comp. Time (s)	
		Random	Tube	Random	Tube	Random	Tube
Original	-	0	0	1	1	-	-
Subsampled & Zero-filled	50	0.5956	0.5863	0.4118	0.4635	-	-
	40	0.6487	0.6481	0.3523	0.3983	-	-
	20	0.7769	0.7710	0.2265	0.2834	-	-
TOUCAN	50	0.0694	0.0728	0.9666	0.9745	12.57	1.444
	40	0.0757	0.0787	0.9596	0.9685	17.61	1.427
	20	0.1805	0.1363	0.8979	0.9330	20.83	1.372
TNN-ADMM	50	0.0303	0.0842	0.9873	0.9768	20.93	28.55
	40	0.0709	0.1639	0.9499	0.9568	29.02	29.80
	20	0.3294	0.3990	0.7799	0.8364	29.76	27.93
TCTF	50	0.0307	0.0311	0.9907	0.9906	7.503	13.36
	40	0.0311	0.0358	0.9905	0.9901	11.49	20.20
	20	0.0651	0.0486	0.9474	0.9871	61.45	62.93
OLSTEC	50	0.1171	0.0573	0.9654	0.9800	46.36	44.75
	40	0.1498	0.0630	0.9529	0.9756	45.81	44.58
	20	0.2362	0.1937	0.8327	0.8765	44.01	42.17
TeCPSGD	50	0.0942	0.1133	0.9384	0.9307	3.527	2.991
	40	0.1035	0.1430	0.9277	0.9059	3.476	2.881
	20	0.1799	0.3307	0.8611	0.7394	2.990	2.551
STC	50	0.4389	-	0.6437	-	20.82	-
	40	0.4754	-	0.9905	-	25.30	-
	20	0.6170	-	0.6663	-	14.05	-

Table 2: Brain fMRI experiment statistics.

TeCPSGD. For the in vivo cardiac perfusion dataset, we set  $\lambda = 0.5$  and  $\mu = 0.0001$  for OLSTEC, and  $\lambda = 0.0001$  and the initial step size to be  $1e5$  for TeCPSGD. The batch t-SVD algorithms are allowed to compute over the data until the difference in NRMSE between iterates is less than  $1e - 4$  or the algorithm exceeds a specified maximum number of iterations.

The experiments are conducted for tubal and random sampling. We compute the NRMSE and mean structural similarity index measures (SSIM) [39] of the reconstructed images along with the total computation times for each algorithm. We show a sample of the reconstruction results in Figs. 7, 8, 9, 10, and 12, along with plots of the NRMSE of each frame of the real  $k$ - $t$  space as the online algorithms process through the data in Figs. 11 and 12.

The results are summarized for the fMRI data in table 2. We note that STC’s poorer reconstruction shows unfolding the tensor can be nonideal, and choosing three matrix unfolding ranks can be challenging. Our experiments show TOUCAN achieves the lowest NRMSE per frame of real  $k$ - $t$  space component among the streaming algorithms; recovery of the phase component is similar. TOUCAN achieves reconstruction in the fewest number of frames, even with only 20% sampling. In the tubal-sampling case, which is most practical in real fMRI collection, TOUCAN’s efficient version is competitive with TCTF or TeCPSGD in reconstruction measures, but takes far less computation time.

When deployed on the highly dynamic in vivo cardiac perfusion data, our method can more rapidly update its subspace estimate during initialization than either OLSTEC or TeCPSGD. We display our results in table 3. Beginning at frame 41, strong breathing motion occurs, and the three algorithms are comparable in their subspace tracking abilities. We display the reconstruction results of frame 53 in Fig. 13 where TOUCAN visually has superior quality.

**6. Discussion & Future Work.** In this paper we presented a novel algorithm for low-tubal-rank tensor completion with stochastic gradient descent on the tensor

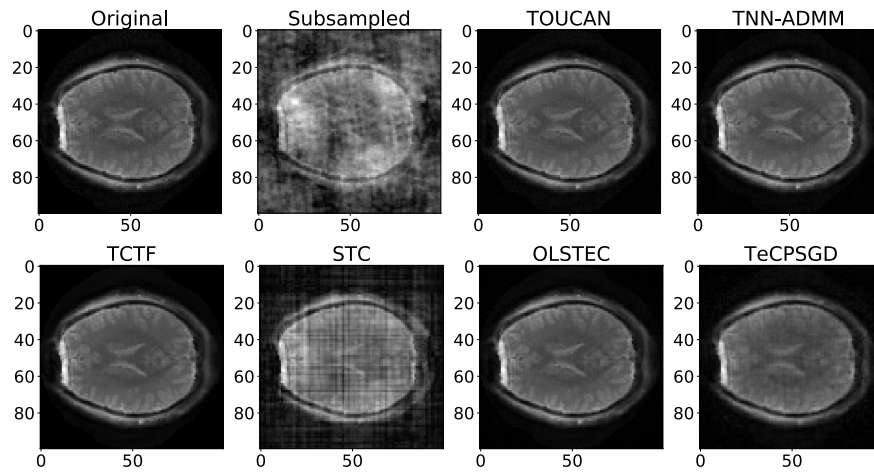


Fig. 7: Reconstructed brain fMRI images from 40% entries.

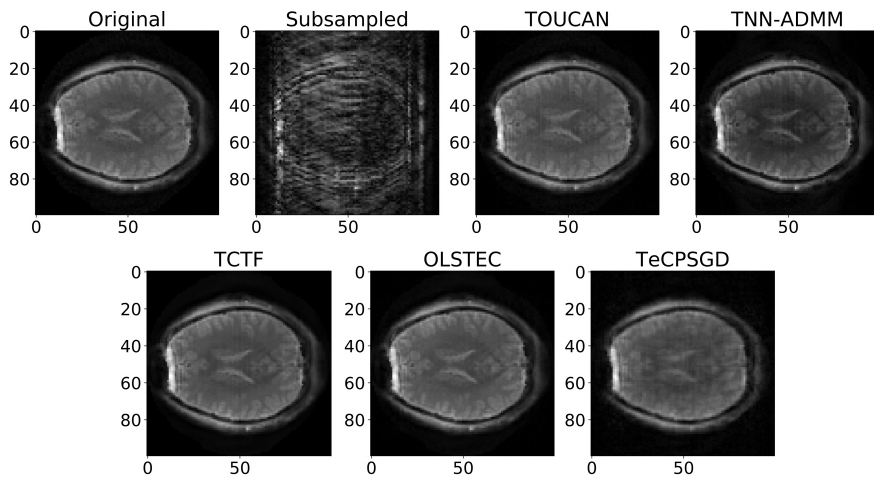


Fig. 8: Reconstructed brain fMRI images from 40% tubes.

Grassmann manifold under the  $t$ -SVD algebraic framework. Our method avoids computing any SVDs, and only needs to update and store a smaller orthonormal tensor and the lateral slice of weights per iteration, leading to a powerful and efficient online algorithm that scales linearly in memory use and computation. TOUCAN naturally extends well-known concepts from matrix algebra to the tensor domain for streaming data under the  $t$ -SVD model, making it practical in big data settings where batch methods would become intractable.

We intend to implement a robust version of TOUCAN for tensor RPCA problems like HSV foreground/background separation. This will also avoid the need to manually remove outliers in the data, as in our chemo-sensing experiments. TOUCAN is practical in many big data problems where the tensor data is inherently oriented, such as time series data, and contains modes with periodic data best captured by the FFT in the  $t$ -SVD framework. However, choosing the best tensor orientation is not always apparent and requires trial and error. While  $t$ -SVD algorithms can leverage periodic

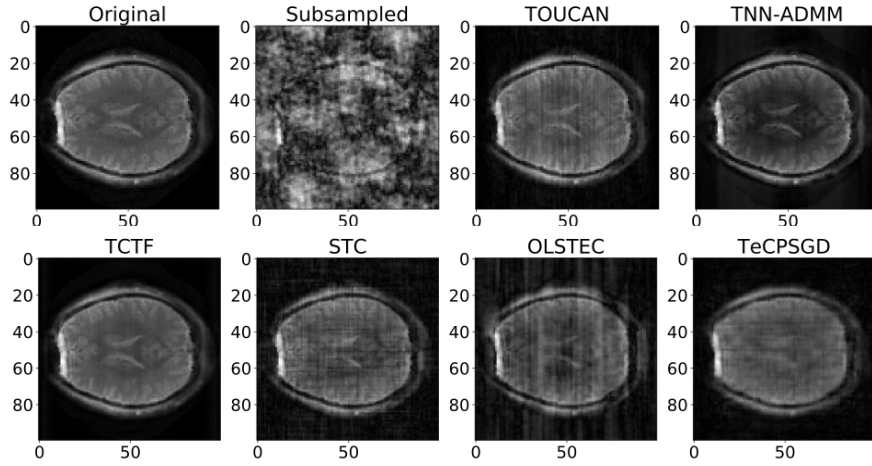


Fig. 9: Reconstructed brain fMRI images from 20% random entries.

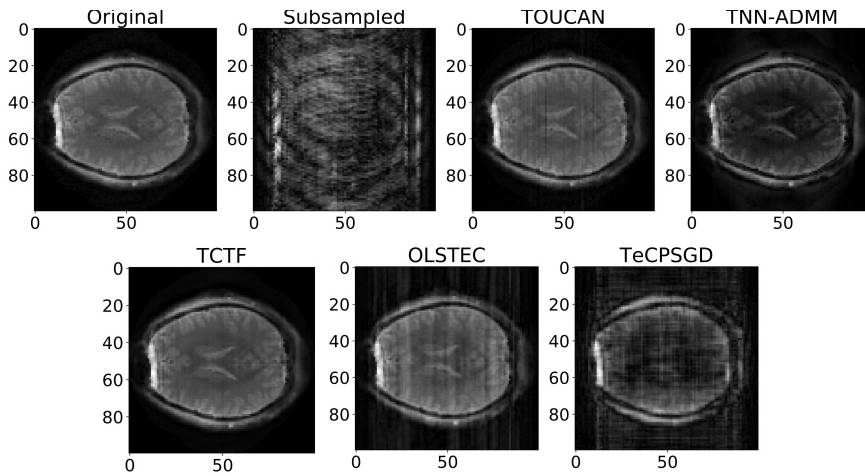
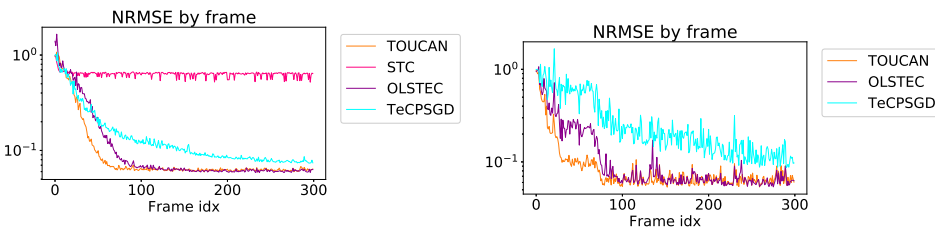


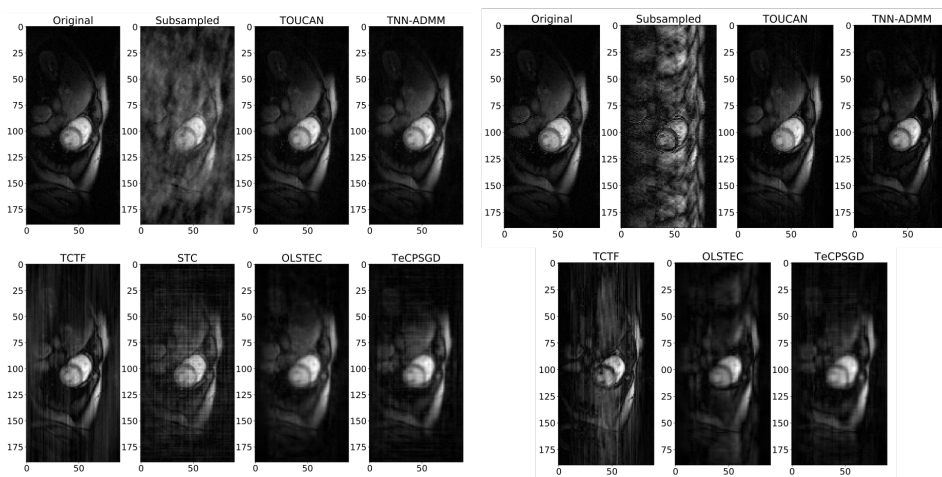
Fig. 10: Reconstructed brain fMRI images from 20% tubes.



(a) From sampling 20% entries uniformly at random.

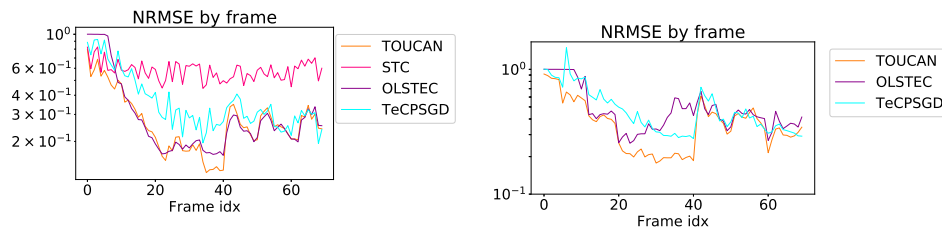
(b) From sampling 20% tubes.

Fig. 11: NRMSE of recovered real component by frame index for brain fMRI dataset.



(a) 40% missing entries at frame 39.

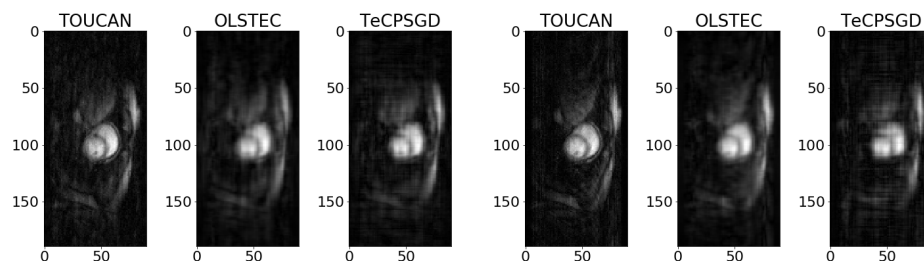
(b) 40% missing tubes at frame 39.



(c) NRMSE of recovered real component by frame index from 40% entries uniformly at random.

(d) NRMSE of recovered real component by frame index from 40% tubes.

Fig. 12: Reconstructed myocardial perfusion images.



(a) 40% missing entries at frame 53.

(b) 40% missing tubes at frame 53.

Fig. 13: Reconstructions of frame 53.

structure in the data, CP models have the advantage of being compatible with any tensor orientation. CP methods may also be preferable when the CP-rank is much smaller than either tensor mode dimension; TOUCAN's memory requirement will grow multiplicatively between  $n_1$ ,  $n_3$ , and  $r$  to store the orthonormal basis, whereas CP methods require only storing three small factor matrices of sizes  $n_1 \times r$ ,  $n_2 \times r$ , and  $n_3 \times r$ . Lastly, t-SVD methods are only useful for imputing missing entries or

	Sample %	NRMSE		SSIM		Comp. Time (s)	
		Random	Tube	Random	Tube	Random	Tube
Original	–	0	0	1	1	–	–
Subsampled & Zero-filled	50	0.5755	0.6108	0.4735	0.5678	–	–
	40	0.6441	0.6750	0.3984	0.5094	–	–
	20	0.7757	0.8196	0.2508	0.3744	–	–
TOUCAN	50	0.2148	0.2475	0.8637	0.8507	1.798	0.8240
	40	0.2633	0.3095	0.8102	0.7800	2.110	0.7325
	20	0.4954	0.6157	0.5623	0.4913	3.132	0.6613
TNN-ADMM	50	0.1144	0.1560	0.9518	0.9350	31.29	29.22
	40	0.1578	0.2334	0.9266	0.8984	32.55	29.06
	20	0.3422	0.5208	0.8214	0.7315	29.88	16.49
TCTF	50	0.3378	0.3827	0.7129	0.7118	11.05	10.51
	40	0.4077	0.4389	0.6384	0.6665	11.13	10.35
	20	0.6245	0.6764	0.4021	0.4316	9.997	10.11
OLSTEC	50	0.3302	0.3632	0.7663	0.7403	14.94	13.75
	40	0.3567	0.4318	0.7260	0.6905	14.17	13.56
	20	0.5251	0.7190	0.5609	0.4507	14.29	13.10
TeCPSGD	50	0.3035	0.3641	0.7709	0.7171	1.289	1.171
	40	0.3425	0.4303	0.7272	0.6547	1.276	1.046
	20	0.5002	0.7362	0.5719	0.2817	1.116	0.9145
STC	50	0.5266	–	0.0474	–	7.456	–
	40	0.5523	–	0.64122	–	6.928	–
	20	0.6755	–	0.5524	–	5.130	–

Table 3: Invivo myocardial perfusion experiment statistics.

identifying gross outliers in the robust setting, but not for recovering interpretable latent factors that may be useful for data analysis. An interesting line of future work would be to develop a novel tensor decomposition agnostic to tensor orientation, has the utility of linear algebra operators in multiway data such as in t-SVD, and enjoys the low memory footprint and latent factor interpretability of CP decompositions.

**Acknowledgments.** We would like to acknowledge the helpful advice of Shuchin Aeron, Jeffrey Fessler, and David Hong during the course of this project. We would also like to thank Amos Cao for sharing the brain fMRI dataset. This work was supported by AFOSR YIP award FA9550-19-1-0026 and NSF BIGDATA award IIS-1838179.

## REFERENCES

- [1] P.-A. ABSIL, R. MAHONY, AND R. SEPULCHRE, *Optimization Algorithms on Matrix Manifolds*, Princeton University Press, Princeton, NJ, USA, 2007.
- [2] E. ACAR, D. M. DUNLAVY, T. G. KOLDA, AND M. MRUP, *Scalable tensor factorizations for incomplete data*, *Chemometrics and Intelligent Laboratory Systems*, 106 (2011), pp. 41 – 56, <https://doi.org/https://doi.org/10.1016/j.chemolab.2010.08.004>, <http://www.sciencedirect.com/science/article/pii/S0169743910001437>. Multiway and Multiset Data Analysis.
- [3] H. AVRON, *Advanced Algorithmic Techniques in Numerical Linear Algebra: Hybridization and Randomization*, PhD thesis, Tel Aviv University, 2010.
- [4] L. BALZANO, R. D. NOWAK, AND B. RECHT, *Online identification and tracking of subspaces from highly incomplete information*, 2010 48th Annual Allerton Conference on Communication, Control, and Computing (Allerton), (2010), pp. 704–711.
- [5] D. BANCO, S. AERON, AND W. S. HOGE, *Sampling and recovery of MRI data using low rank tensor models*, in 2016 38th Annual International Conference of the IEEE Engineering in Medicine and Biology Society (EMBC), Aug 2016, pp. 448–452, <https://doi.org/10.1109/EMBC.2016.7590736>.
- [6] D. BERTSEKAS, *Incremental gradient, subgradient, and proximal methods for convex optimization: A survey*, *Optimization*, 2010 (2015).
- [7] E. J. CANDÈS AND B. RECHT, *Exact matrix completion via convex optimization*, *Foundations of Computational Mathematics*, 9 (2009), p. 717, <https://doi.org/10.1007/s10208-009-9045-5>, <https://doi.org/10.1007/s10208-009-9045-5>.

- [8] E. J. CANDÈS AND B. RECHT, *Exact matrix completion via convex optimization*, Foundations of Computational Mathematics, 9 (2009), p. 717, <https://doi.org/10.1007/s10208-009-9045-5>, <https://doi.org/10.1007/s10208-009-9045-5>.
- [9] L. CANYI, J. FENG, Y. CHEN, W. LIU, Z. LIN, AND S. YAN, *Tensor robust principal component analysis with a new tensor nuclear norm*, IEEE Transactions on Pattern Analysis and Machine Intelligence, PP (2018), <https://doi.org/10.1109/TPAMI.2019.2891760>.
- [10] V. DE SILVA AND L. LIM, *Tensor rank and the ill-posedness of the best low-rank approximation problem*, SIAM Journal on Matrix Analysis and Applications, 30 (2008), pp. 1084–1127, <https://doi.org/10.1137/06066518X>, <https://doi.org/10.1137/06066518X>, <https://arxiv.org/abs/https://doi.org/10.1137/06066518X>.
- [11] M. E. KILMER AND C. D. MARTIN, *Factorization strategies for third-order tensors*, Linear Algebra and Its Applications, 435 (2011), <https://doi.org/10.1016/j.laa.2010.09.020>.
- [12] A. EDELMAN, T. ARIAS, AND S. SMITH, *The geometry of algorithms with orthogonality constraints*, SIAM Journal on Matrix Analysis and Applications, 20 (1998), pp. 303–353, <https://doi.org/10.1137/S0895479895290954>, <https://doi.org/10.1137/S0895479895290954>, <https://arxiv.org/abs/https://doi.org/10.1137/S0895479895290954>.
- [13] H. FAN, Y. CHEN, Y. GUO, H. ZHANG, AND G. KUANG, *Hyperspectral image restoration using low-rank tensor recovery*, IEEE Journal of Selected Topics in Applied Earth Observations and Remote Sensing, 10 (2017), pp. 4589–4604, <https://doi.org/10.1109/JSTARS.2017.2714338>.
- [14] H. FAN, C. LI, Y. GUO, G. KUANG, AND J. MA, *Spatialspectral total variation regularized low-rank tensor decomposition for hyperspectral image denoising*, IEEE Transactions on Geoscience and Remote Sensing, 56 (2018), pp. 6196–6213, <https://doi.org/10.1109/TGRS.2018.2833473>.
- [15] D. W. FLETCHER-HOLMES AND A. R. HARVEY, *Real-time imaging with a hyperspectral fovea*, Journal of Optics A: Pure and Applied Optics, 7 (2005), pp. S298–S302, <https://doi.org/10.1088/1464-4258/7/6/007>, <https://doi.org/10.1088%2F1464-4258%2F7%2F6%2F007>.
- [16] K. GILMAN AND L. BALZANO, *Online tensor completion and tracking of free submodules with the  $t$ -SVD*, in 2020 IEEE 45th International Conference on Acoustics, Speech, and Signal Processing (ICASSP), 2020.
- [17] J. GIRSON AND S. AERON, *Tensor completion via optimization on the product of matrix manifolds*, in 2015 IEEE 6th International Workshop on Computational Advances in Multi-Sensor Adaptive Processing (CAMSAP), Dec 2015, pp. 177–180, <https://doi.org/10.1109/CAMSAP.2015.7383765>.
- [18] E. GUJRAL, R. PASRICHA, AND E. E. PAPALEXAKIS, *SamBaTen: Sampling-based Batch Incremental Tensor Decomposition*, pp. 387–395, <https://doi.org/10.1137/1.9781611975321.44>, <https://epubs.siam.org/doi/abs/10.1137/1.9781611975321.44>, <https://arxiv.org/abs/https://epubs.siam.org/doi/pdf/10.1137/1.9781611975321.44>.
- [19] P. JAIN AND S. OH, *Provable tensor factorization with missing data*, in Proceedings of the 27th International Conference on Neural Information Processing Systems - Volume 1, NIPS'14, Cambridge, MA, USA, 2014, MIT Press, pp. 1431–1439, <http://dl.acm.org/citation.cfm?id=2968826.2968986>.
- [20] H. KASAI, *Online low-rank tensor subspace tracking from incomplete data by cp decomposition using recursive least squares*, in 2016 IEEE International Conference on Acoustics, Speech and Signal Processing (ICASSP), March 2016, pp. 2519–2523, <https://doi.org/10.1109/ICASSP.2016.7472131>.
- [21] M. KILMER, K. BRAMAN, N. HAO, AND R. HOOVER, *Third-order tensors as operators on matrices: A theoretical and computational framework with applications in imaging*, SIAM Journal on Matrix Analysis and Applications, 34 (2013), pp. 148–172, <https://doi.org/10.1137/110837711>, <https://doi.org/10.1137/110837711>, <https://arxiv.org/abs/https://doi.org/10.1137/110837711>.
- [22] T. KOLDA AND B. BADER, *Tensor decompositions and applications*, SIAM Review, 51 (2009), pp. 455–500, <https://doi.org/10.1137/07070111X>, <https://doi.org/10.1137/07070111X>, <https://arxiv.org/abs/https://doi.org/10.1137/07070111X>.
- [23] T. G. KOLDA AND D. HONG, *Stochastic gradients for large-scale tensor decomposition*. arXiv, June 2019, <https://arxiv.org/abs/1906.01687>. submitted for publication.
- [24] P. KROONENBERG, *Applied Multiway Data Analysis*, vol. 702, 01 2008, <https://doi.org/10.1002/9780470238004>.
- [25] S. G. LINGALA, Y. HU, E. DiBELLA, AND M. JACOB, *Accelerated dynamic mri exploiting sparsity and low-rank structure:  $k$ - $t$  SLR*, IEEE Transactions on Medical Imaging, 30 (2011), pp. 1042–1054, <https://doi.org/10.1109/TMI.2010.2100850>.
- [26] J. LIU, P. MUSIALSKI, P. WONKA, AND J. YE, *Tensor completion for estimating missing values*



- in visual data*, IEEE Transactions on Pattern Analysis and Machine Intelligence, 35 (2013), pp. 208–220, <https://doi.org/10.1109/TPAMI.2012.39>.
- [27] C. MA, X. YANG, AND H. WANG, *Randomized online cp decomposition*, in 2018 Tenth International Conference on Advanced Computational Intelligence (ICACI), March 2018, pp. 414–419, <https://doi.org/10.1109/ICACI.2018.8377495>.
- [28] T. MAEHARA, K. HAYASHI, AND K.-I. KAWARABAYASHI, *Expected tensor decomposition with stochastic gradient descent*, in Proceedings of the Thirtieth AAAI Conference on Artificial Intelligence, AAAI16, AAAI Press, 2016, p. 19191925.
- [29] M. MARDANI, G. MATEOS, AND G. B. GIANNAKIS, *Subspace learning and imputation for streaming big data matrices and tensors*, IEEE Transactions on Signal Processing, 63 (2015), pp. 2663–2677, <https://doi.org/10.1109/TSP.2015.2417491>.
- [30] C. MARTIN, R. SHAFER, AND B. LARUE, *An order- $p$  tensor factorization with applications in imaging*, SIAM Journal on Scientific Computing, 35 (2013), pp. A474–A490, <https://doi.org/10.1137/110841229>, <https://arxiv.org/abs/https://doi.org/10.1137/110841229>.
- [31] C. D. MARTIN, R. SHAFER, AND B. LARUE, *An order- $p$  tensor factorization with applications in imaging*, SIAM Journal on Scientific Computing, 35 (2013), pp. A474–A490, <https://doi.org/10.1137/110841229>, <https://arxiv.org/abs/https://doi.org/10.1137/110841229>.
- [32] D. NION AND N. D. SIDIROPOULOS, *Adaptive algorithms to track the parafac decomposition of a third-order tensor*, IEEE Transactions on Signal Processing, 57 (2009), pp. 2299–2310, <https://doi.org/10.1109/TSP.2009.2016885>.
- [33] K. B. PETERSEN AND M. S. PEDERSEN, *The matrix cookbook*, 2012, <https://www.math.uwaterloo.ca/~hwolkowi/matrixcookbook.pdf>.
- [34] J. POTHIER, J. GIRSON, AND S. AERON, *An algorithm for online tensor prediction*, 2015, <https://arxiv.org/abs/1507.07974>.
- [35] Q. SONG, H. GE, J. CAVERLEE, AND X. HU, *Tensor completion algorithms in big data analytics*, ACM Transactions on Knowledge Discovery from Data, 13 (2017), <https://doi.org/10.1145/3278607>.
- [36] M. VANDECAPPELLE, N. VERVLIET, AND L. DE LATHAUWER, *Nonlinear least squares updating of the canonical polyadic decomposition*, in 2017 25th European Signal Processing Conference (EUSIPCO), Aug 2017, pp. 663–667, <https://doi.org/10.23919/EUSIPCO.2017.8081290>.
- [37] A. VERGARA, J. FONOLLOSA, J. MAHIQUES, M. TRINCAVELLI, N. RULKOV, AND R. HUERTA, *On the performance of gas sensor arrays in open sampling systems using inhibitory support vector machines*, Sensors and Actuators B: Chemical, 185 (2013), pp. 462 – 477, <https://doi.org/https://doi.org/10.1016/j.snb.2013.05.027>, <http://www.sciencedirect.com/science/article/pii/S092540051300590X>.
- [38] T. WANG, Z. ZHU, AND E. BLASCH, *Bio-inspired adaptive hyperspectral imaging for real-time target tracking*, IEEE Sensors Journal, 10 (2010), pp. 647–654, <https://doi.org/10.1109/JSEN.2009.2038657>.
- [39] Z. WANG, A. C. BOVIK, H. R. SHEIKH, AND E. P. SIMONCELLI, *Image quality assessment: From error visibility to structural similarity*, Trans. Img. Proc., 13 (2004), pp. 600–612, <https://doi.org/10.1109/TIP.2003.819861>, <http://dx.doi.org/10.1109/TIP.2003.819861>.
- [40] D. ZHANG AND L. BALZANO, *Global convergence of a grassmannian gradient descent algorithm for subspace estimation*, in AISTATS, 2015.
- [41] Z. ZHANG AND S. AERON, *Exact tensor completion using  $t$ -SVD*, IEEE Transactions on Signal Processing, 65 (2017), pp. 1511–1526, <https://doi.org/10.1109/TSP.2016.2639466>.
- [42] Z. ZHANG, G. ELY, S. AERON, N. HAO, AND M. KILMER, *Novel methods for multilinear data completion and de-noising based on tensor-svd*, in 2014 IEEE Conference on Computer Vision and Pattern Recognition, June 2014, pp. 3842–3849, <https://doi.org/10.1109/CVPR.2014.485>.
- [43] Z. ZHANG, D. LIU, S. AERON, AND A. VETRO, *An online tensor robust PCA algorithm for sequential 2D data*, in 2016 IEEE International Conference on Acoustics, Speech and Signal Processing (ICASSP), March 2016, pp. 2434–2438, <https://doi.org/10.1109/ICASSP.2016.7472114>.
- [44] P. ZHOU, C. LU, Z. LIN, AND C. ZHANG, *Tensor factorization for low-rank tensor completion*, IEEE Transactions on Image Processing, 27 (2018), pp. 1152–1163, <https://doi.org/10.1109/TIP.2017.2762595>.